>Geochemical and hydrological model for bauxite residue sand. >Combined hydrogeochemical simulation of bauxite residue sand under field conditions, in 2D, heterogeneous domomain. >Evaluation of management practise for the amelioration of bauxite residue sand as substrate for plant growth.

This manuscript illustrates an innovative application of detailed hydrogeochemical modelling to the field of bauxite residue management. A recently developed simulation tool that combines geochemical reaction calculations in PHREEQC with variably saturated flow and transport processes in COMSOL was employed to investigate the evolution of water availability and water quality in fertigated and amended bauxite residue sand as response to rainfall leaching. The level of detail in flow and reactions calculations is novel to studies of residue management and rehabilitation. Due to the general applicability, the employed simulation and parameterization techniques are of interest to a broad audience in the field of mining waste management.

Predictive Hydrogeochemical Modelling of Bauxite Residue Sand in Field Conditions

Laurin Wissmeier[*,a], David A. Barry[a] and Ian R. Phillips[b]

[a] Ecole Polytechnique Fédérale de Lausanne (EPFL)
Faculté de l'Environnement Naturel, Architectural et Construit (ENAC)
Laboratoire de Technologie Ecologique
Station 2, 1015 Lausanne, Switzerland

[b] Mining Environmental Group
Alcoa of Australia Ltd.
PO Box 172 Pinjarra WA 6208, Australia

Revised and resubmitted to *Journal of Hazardous Materials*

19 April 2011

∗ Author to whom all correspondence should be addressed. Telephone: +49 761 211 138-0, facsimile: +49 761 211 138-29.
E-mail addresses: laurin.wissmeier@epfl.ch (L. Wissmeier), andrew.barry@epfl.ch (D.A. Barry),
ian.phillips@alcoa.com.au (I.R. Phillips)

1   **Abstract**

2   The suitability of residue sand (the coarse fraction remaining from Bayer's process of bauxite

3   refining) for constructing the surface cover of closed bauxite residue storage areas was

4   investigated. Specifically, its properties as a medium for plant growth are of interest to ensure

5   residue sand can support a sustainable ecosystem following site closure. The geochemical

6   evolution of the residue sand under field conditions, its plant nutrient status and soil moisture

7   retention were studied by integrated modelling of geochemical and hydrological processes.

8   For the parameterization of mineral reactions, amounts and reaction kinetics of the mineral

9   phases natron, calcite, tricalcium aluminate, sodalite, muscovite and analcime were derived

10   from measured acid neutralization curves. The effective exchange capacity for ion adsorption

11   was measured using three independent exchange methods. The geochemical model, which

12   accounts for mineral reactions, cation exchange and activity corrected solution speciation,

13   was formulated in the geochemical modelling framework PHREEQC, and partially validated

14   in a saturated flow column experiment. For the integration of variably saturated flow with

15   multi-component solute transport in heterogeneous 2D domains, a coupling of PHREEQC

16   with the multi-purpose finite-element solver COMSOL was established. The integrated

17   hydrogeochemical model was applied to predict water availability and quality in a vertical

18   flow lysimeter and a cover design for a storage facility using measured time series of rainfall

19   and evaporation from southwest Western Australia. In both scenarios the sand was fertigated

20   and gypsum-amended. Results show poor long-term retention of fertilizer ions and buffering

21   of the pH around 10 for more than 5 years of leaching. It was concluded that fertigation,

22   gypsum amendment and rainfall leaching alone were insufficient to render the geochemical

23   conditions of residue sand suitable for optimal plant growth within the given timeframe. The

24   surface cover simulation demonstrates that the soil moisture status in the residue sand can be

25   ameliorated by an appropriate design of the cover layer with respect to thickness, slope and

26   distance between lateral drains.

27   **Keywords**

28   bauxite refining residue, geochemical modelling, PHREEQC, IPhreeqc, COMSOL, PEST,

29   mineral reactions, cation exchange, vadose zone, variable saturation, revegetation, waste

30   management

1   Introduction

The worldwide production of alumina (83.3 Mt in 2008 [1]) is associated with the creation of about 120 Mt of problematic bauxite refining residues each year [2]. In Western Australia, where about a third of the alumina on the global market is produced [3], the residue is disposed of in large impoundments close to the refineries, where it is left to drain and air-dry (dry-stacking) [4, 5]. In anticipation of future storage capacity limits, the bauxite refining industry seeks safe and economically feasible strategies of sustainable storage site closure. Important objectives for successful closure are [6-11]

- reduction of infiltration into the underlying residue;
- dust control;
- erosion control;
- minimization of the need for future reworking; and,
- limitation of the visual obtrusiveness.

These objectives could be achieved by a self-sustaining vegetation cover on top of residue storage areas. Since the reuse of residue sand (the coarse fraction of the residue; characteristic grain size $> 10^{-4}$ m) as a medium for plant growth would greatly reduce the costs of revegetation, research into its suitability as a substrate has been recently intensified. However, plant productivity on residue sand is impeded by the geochemical conditions that reactions of highly unstable minerals impose on the soil solution [12]. Characteristic properties of the residue sand are [7, 11, 13-15]:

- high pH (10-12.5);
- high total alkalinity (ca. 20 meq l^{-1});
- high electrical conductivity (ca. 1500 μS cm^{-1}); and,
- high exchangeable sodium percentage (close to 100%).

4

55 Besides the general geochemical conditions, the plant nutrient status in the residue sand plays

56 a critical role for the long-term revegetation success [8, 12, 15]. Chen et al. [16, 17] therefore

57 investigated the retention of major nutrients in residue sand after additions of a standard

58 ammonium-phosphate fertilizer. In [17], they specifically focused on the loss of ammonia

59 (NH_3) due to volatilization. Fractionation and availability of micronutrients such as B, Cu,

60 Fe, Mn and Zn in residue sand was examined by Thiyagarajan et al. [10]. Motivated by the

61 observed Mn deficiency of plants on residue sand, Gherardi and Rengel [13] investigated the

62 detailed fractionation of this essential nutrient. Phillips and Chen [14] studied ion adsorption

63 onto variable charge adsorption sites as the main fractionating process for micronutrients.

64 To date the interference on adsorption sites of fertilizer retention and mineral dissolution

65 reactions as result of ion competition remains unclear. More importantly, the influence of soil

66 moisture dynamics and solute transport on the geochemical factors that determine sand

67 fertility in field conditions is largely unknown. Under natural leaching conditions, imposed

68 by rainfall and evaporation, geochemical processes of ion adsorption and mineral dissolution

69 are controlled by variably saturated soil moisture movement and influenced by changes in

70 local ion concentrations due to solute transport [18-21]. Therefore, flow and transport are

71 crucial components in the assessment of the long-term efficiency of management strategies,

72 such as fertilizer addition or gypsum amendment [22-24]. Besides its importance for ion

73 transport and solution reactivity, water availability plays a key role in residue sand fertility.

74 Integrated hydrogeochemical modelling is a powerful tool to investigate simultaneous

75 geochemical reactions, such as mineral reactions and ion adsorption, considering their

76 dependency on soil moisture dynamics and solute transport [25-28]. Here, we present the first

77 interdisciplinary modelling of bauxite refining residue sand by combining geochemical

78 reactions with rainfall- and evaporation-induced variably saturated flow in 2D heterogeneous

79 domains. The objectives are (1) to develop and parameterise submodels for the geochemical

5

80   and hydrological processes in residue sand, and (2) to predict the long-term effect of

81   fertilization and gypsum amendment on residue sand fertility in field conditions through

82   integrated hydrogeochemical modelling.

83   The paper is structured as follows: A geochemical model for residue sand is established in

84   Section 2. Mineral reactions are derived from measured acid neutralization curves in

85   combination with speciation modelling and linked parameter optimization. Ion adsorption is

86   considered by a cation exchange process using independent measurements to determine the

87   effective exchange capacity. The model is formulated in the geochemical modelling

88   framework PHREEQC [29] and is partially validated against results from saturated-flow

89   column experiments. Section 3 presents the hydraulic properties of residue sand with

90   relevance to hydrological modelling. The software for coupled simulations of geochemistry

91   and unsaturated hydrological processes is described briefly in Section 4. Details of novel

92   model features and the implementation of atmospheric boundary conditions are provided in

93   Appendices A-C. Section 5 describes the meteorological conditions at ALCOA's Pinjarra

94   Alumina Refinery in south-west Western Australia where the model is applied. Results from

95   predictive simulations of a constructed lysimeter and a surface cover design for residue

96   storage areas are presented in Sections 6 and 7. The main model uncertainties are discussed in

97   Section 0 together with implications for residue management. Conclusions with respect to the

98   fertilizer addition and gypsum amendment as well as the overall suitability of residue sand as

99   a plant growth substrate are drawn in Section 9.

2 Geochemical Model

2.1 Solid Phase Properties

The geochemistry of fresh, untreated residue sand is dominated by dissolution of readily soluble salts and minerals [e.g., 30]. In order to simulate the geochemical conditions as a response to fertigation, gypsum amendment and rainfall leaching, detailed knowledge of the stoichiometry, quantity and reactivity of the soluble minerals is required. Taylor and Pearson [31] found 58% quartz, 22% hematite, 7% gibbsite, 5% goethite, 1% anatase, 1% muscovite and 0.3% boehmite as the major mineral fractions in residue sand. Because of their low solubility and/or slow reactions kinetics, these major mineral fractions contribute little to the overall geochemical conditions in the soil solution. Instead, highly reactive salts such as natron ($Na_2CO_3:10H_2O$) , calcite ($CaCO_3$), tricalcium aluminate (TCA; $Ca_3Al_2O_6$) [32-34] and the desilication product (DSP; e.g., sodalite $Na_8(AlSiO_4)_6Cl_2$) [15, 35-40] are responsible for the high pH and large acid neutralization capacity of the bauxite residue [30, 41]. Although identified qualitatively by XRD [30], the proportions of these minerals in residue sand is currently unknown.

For the parameterization of the geochemical model, the reactive mineral proportions were found by matching measured acid neutralization curves with simulations performed in PHREEQC. In this approach, the solution pH was regarded as a master variable and an integrated measure for the overall geochemical conditions [42]. Similar to the procedure used by Snars and Gilkes [30], buffering plateaus are associated with the dissolution of distinct mineral phases and the persistence of buffering regions is related to the amount of the minerals in the mineral assembly.

Acid neutralization was measured over the pH range of 2 – 12. 30 g of residue sand (ø < 2 mm, oven-dried for > 2 d at 50°C) were placed into a series of 20 polystyrol screw-lid

124   beakers (190 ml, Semadeni). A 0.5 M HCl solution was added to the beakers in quantities

125   ranging from 0 to 14.25 ml in steps of 0.75 ml. The beakers were made up to volume using

126   Milli-Q deionised water to achieve a liquid to solid ratio of 5:1 by weight. Samples were

127   thoroughly mixed (20 rpm) using an end-over-end shaker. Excessive gas phase equilibration

128   was avoided by reducing the empty volume in each beaker to ca. 20 ml. The pH of each

129   suspension was recorded 2, 4, 24, 48, 72 and 96 h after acid addition using a robotic

130   titrosampler (Metrohm 855) with a platinum electrode (Metrohm 6.0257.000 Aquatrode

131   Plus).

132   **Fig. 1: Measured (a) and simulated acid neutralization curves at thermodynamic equilibrium (b) and including the**
133   **kinetic dissolution of TCA and sodalite (c).**

134   Acid neutralization curves show distinct buffering plateaus at pH 7 and pH 4 and a less

135   pronounced buffering region around pH 9-10 (Fig. 1a). Over time, acid consumption

136   increased due to kinetic mineral dissolution, giving the impression of a moving pH front.

137   After 72 h, the pH stabilised, suggesting that readily soluble alkalinity was consumed and that

138   fast kinetic reactions attained quasi-equilibrium. The extent of further buffering due to slowly

139   reacting minerals remains uncertain. However, over the time scale examined, the acid

140   neutralisation curves provide reliable information on the effects of acid on the geochemical

141   behaviour of residue sand.

142   In the first step of the model development, the acid neutralization at 2 h was reproduced by

143   simulating the solution in equilibrium with the fast reacting minerals natron, calcite,

144   muscovite and analcime. The latter two minerals provide buffering around pH 4 and are

145   therefore of minor importance under conditions typically observed for residue sand deposited

146   in the field (pH > 7). The quantity of natron and calcite were optimized to match the

147   measured acid neutralization curve through coupling PHREEQC with the model-independent

148   parameter estimation software PEST (version 12) [43]. The second step in model

149   development introduced the minerals TCA and sodalite, whose quantities were optimised in

150   PHREEQC to reproduce the acid neutralisation curve observed after 96 h of reaction time.

151   The mineral sodalite was included as a surrogate to represent the variety of components in the

152   desilication product [44]. Similarly, TCA represents the mineral group of calcium aluminates.

153   Since the buffering capacity around pH 4 was not exhausted during the experiment, the

154   amount of muscovite was estimated from the mineralogical data of Taylor and Pearson [31]

155   given above. The amount of sodium (Na) in fresh residue sand that is not accounted for by

156   natron and sodalite was attributed to analcime. Reactive Na as measured by leach testing over

157   a range of pH from 0.8 to 11.8 (data not shown) amounts to 5.415×10^{-3} g g^{-1}. Measured and

158   simulated acid neutralization curves at 2 and 96 h are presented in Fig. 1b. In a third step of

159   model development, acid neutralization between 2 and 96 h was attributed to kinetic

160   dissolution of TCA and sodalite. In agreement with transition state theory [e.g., 45], the rate

161   expression

$$s_i \frac{dm_i}{dt} = k\,(1-\Omega)\,A\left(\frac{M}{M_0}\right)^{\frac{2}{3}}, \tag{1}$$

162   given by the PHREEQC manual [29] was employed. In Eq. (1), s_i is the stoichiometric factor

163   of component i in the mineral phase, m_i is the quantity of component i in the liquid phase

164   (mol), k is the rate constant (mol m^{-2} s^{-1}), Ω is the saturation ratio and A is the mineral surface

165   area (m^2). The factor $\left(\frac{M}{M_0}\right)^{\frac{2}{3}}$ accounts for the change in mineral surface with dissolution

166   progress for spherical mineral grains, where M is the current amount of mineral (mol) and M_0

167   is the initial amount of mineral (mol). The saturation ratio Ω is defined by

$$\Omega = \frac{\prod a_i^{s_i}}{K}, \tag{2}$$

168 where a_i is the activity of component i and K is the equilibrium constant of the

169 dissolution/precipitation reaction. The reactive surface area A of the mineral phases was set

170 equal to the total surface area of residue sand. The total surface area (2.708×10^{-2} m^2 g^{-1}) was

171 calculated from laser diffraction particle analysis (LS™ 13 320, Beckman Coulter) assuming

172 spherical particles (see Appendix D). The rate constant k and the initial amount M_0 were

173 estimated by matching all measured acid neutralization curves at all time periods between 2

174 and 96 h of reaction by the coupling of PHREEQC and PEST (Fig. 1c).The derived mineral

175 properties for subsequent modelling are summarized in Table 1.

176 **Table 1: Mineral properties of residue sand as derived from acid neutralization.**

Mineral name Reaction formula	Equilibrium constant	Rate constant (mol m^{-2} s^{-1})	Relative amount (mol kg$_{solid}^{-1}$)
Calcite $CaCO_3 = CO_3^{-2} + Ca^{+2}$	$10^{-8.48\,a}$	-	2.531×10^{-2}
Natron $Na_2CO_3{:}10H_2O = 2Na^+ + CO_3^{-2} + 10H_2O$	$10^{-1.311\,a}$	-	3.991×10^{-2}
Muscovite $KAl_3Si_3O_{10}(OH)_2 + 10H^+ = K^+ + 3Al^{+3} + 3H_4SiO_4$	$10^{14\,b}$	-	2.511×10^{-2}
Analcime $NaAlSi_2O_6{:}H_2O + H_2O + 4H^+ = Na^+ + Al^{+3} + 2H_4SiO_4$	$10^{6.719\,a}$	-	3.054×10^{-2}
Sodalite $Na_8(AlSiO_4)_6Cl_2 + 24H_2O = 8Na^+ + 6Al(OH)_4^- + 6H_4SiO_4 + 2Cl^-$	$10^{-55.89\,c}$	3.405×10^{-9}	4.237×10^{-3}
TCA $Ca_3Al_2O_6 + 12H^+ = 3Ca^{+2} + 2Al^{+3} + 6H_2O$	$10^{74\,d}$	7.484×10^{-10}	5.569×10^{-3}

177 [a] minteq.dat (distributed with PHREEQC), [b] sit.dat (distributed with PHREEQC), [c] calculated from
178 thermodynamic data in Komada et al. [46], [d] Khaitan et al. [34]

179 The results in Fig. 1b show excellent agreement between the simulated and measured acid

180 neutralization curves after 2 h using the fast reacting minerals natron and calcite to represent

181   the buffering regions at pH 7 and around pH 10. The correlation coefficient according to

182   Cooley and Naff [47] amounts to 0.995. The measured decline in pH with the addition of 2

183   mmol HCl as well as the exhaustion of the buffering capacity after addition of 7 mmol HCl is

184   well reproduced. However, the pH is overestimated by about one pH unit in the strongly

185   alkaline region (pH > 9), whereas it is slightly underestimated for the addition of 2-7 mmol

186   acid. This is reflected also by the lower correlation coefficient of 0.973.The simulation of

187   kinetic pH buffering in Fig. 1c, with an overall correlation coefficient of 0.982, shows that

188   simple rate expressions are sufficient to produce reasonable agreement of this time-dependent

189   process. Since the field pH remains always in the alkaline range, the mismatch between

190   measured and simulated pH below 7 is of lower importance.

191   *2.2   Adsorption Properties*

192   The adsorption of fertilizers as result of cation exchange is critical to the understanding of

193   nutrient retention , which is crucial for plant growth. The effective cation exchange capacity

194   (CEC) of residue was measured using three independent methods: (i) the method of Ca-Mg

195   exchange for soils containing salts, carbonates and zeolites [48], (ii) the unbuffered salt

196   extraction method at field pH [modified after 49, in 50], and (iii) the cobalt hexamine

197   compulsive exchange method [51]. Measurements were taken from three replicates using

198   each method.

199   Prior to testing, the residue sand was washed to avoid errors due to the dissolution of readily

200   soluble salts. 40 g of oven-dried sand (50°C, > 2 d, ø < 0.5 mm) were weighed into a 250 ml

201   Nalgene bottle, after which 200 ml of water (Milli-Q) was added to achieve a liquid to solid

202   ratio of 5:1. The bottles were shaken end-over-end for 1 h and centrifuged at 2×10^3 rpm for

203   30 min. The clear supernatant was manually decanted and care was taken not to lose any of

204   the fine material that deposited as a red layer on top of the coarse sand. Subsequently, the

205   bottles were made up to volume. The washing procedure was repeated 10 times, during which

206   the electrical conductivity decreased from 1513 $\mu S \ cm^{-1}$ to 53 $\mu S \ cm^{-1}$ indicating the removal

207   of the most soluble mineral fractions [52].

208   **Table 2: Cation exchange capacity on washed residue sand.**

Method	CEC (cmol kg_{solid}^{-1})
(i): Ca-Mg	0.66
(ii): NH_4-K	1.21
(iii): $Co(NH_3)_6Cl_3$	0.72

209   Each of the three methods yielded CEC values of the same order of magnitude (Table 2).

210   However, the value from the NH_4-K exchange method was about twice as high as results

211   from the other two methods. The Ca-Mg exchange method and the cobalt hexamine method

212   lower the native pH of the residue sand. This may decrease the number of pH-dependent

213   surface sites, which could explain the lower measured exchange capacity. In the following

214   model applications the arithmetic mean of all three methods (CEC: 0.86 cmol kg_{solid}^{-1}) was

215   used as the effective exchange capacity of residue sand. For the definition of ion association

216   reactions, PHREEQC's default database *phreeqc.dat* was employed.

217   *2.3   Column Study for Model Validation*

218   Before modelling fertiliser transport under field conditions, the model representation of

219   geochemical processes under controlled laboratory conditions was evaluated. A column

220   leaching experiment in saturated upward flow conditions was performed to provide partial

221   validation of the geochemical model by comparison of simulated and measured pH, electrical

222   conductivity and element concentrations in the outflow. The experimental setup is displayed

223   in Fig. 2.

224   **Fig. 2: Upward flow column experiment.**

225   In order to achieve homogenous packing, the untreated, oven-dried residue sand ($50°C$, > 2 d,

226   ø < 2 mm) was poured into a glass column in portions of 5 ± 2 g while a head of 2-5 cm of

227   Milli-Q water was maintained in the column [wet packing, 53]. This packing achieved a final

228   bulk density of about 1.56 g cm^{-3}. No particle separation was observed in the sand column

229   after packing. Deionised water was supplied at the base (inflow) of the vertical column at a

230   constant flux (15.03 cm^3 min^{-1}) using a peristaltic pump (Ismatec MCP). The discharge was

231   collected above the outflow plug in 75.15 cm^3 aliquots, and retained for analysis. Column

232   properties are shown in Table 3.

233   **Table 3: Column properties.**

Property	Value
Column diameter	40 mm
Column length	600 mm
Flux	15.03 cm^3 min^{-1}
Porosity	0.43
Fill volume	600 cm^3

234   The leaching experiment was performed in three replicates (Series I, II and III). Automated

235   measurements of pH and electrical conductivity in the outflow aliquots were taken using a

236   robotic titrosampler (Metrohm 855 Robotic Titrosampler) in combination with appropriate

237   electrodes (Metrohm 6.0257.000 Aquatrode Plus, Metrohm 712 Conductometer with

238   Metrohm 6.0912.110). For alkalinity measurements, samples were immediately titrated to pH

239   4.3 with 0.01 M HCl using an automated titrator (Metrohm 800 Dosino). The CO_2 gas

240   saturation was calculated from pH and alkalinity measurements using PHREEQC by

241   attribution of alkalinity to carbonate species, protons and hydroxyl ions. Major element

242   concentrations were measured in the outflow of Series III using an ICP-OES instrument

243 (Perkin Elmer Optima 3300 DV). Samples were filtered (Whatman Spartan 30 0.45 μm),

244 acidified to pH < 2 using HCl and stored at 4°C prior to analysis.

245 The column experiment was simulated using PHREEQC's 1D-transport capabilities and the

246 geochemical properties that were derived in Sections 2.1 and 2.2. The initial pore water and

247 the inflowing solution were assumed to be in equilibrium with atmospheric CO_2 and O_2. Ion

248 diffusion and physical dispersivity were estimated as 3×10^{-10} m^2 s^{-1} and 10^{-1} m, respectively.

249 Flushing the column with 100 pore volumes corresponds to approximately 35 y of rainfall

250 leaching in the climatic conditions of Western Australia with an estimated annual effective

251 recharge of 600 mm (see Section 5). Measured and simulated pH, alkalinity, electrical

252 conductivity (EC) and CO_2 saturation in the discharge are presented in

253 Fig. 3.

254 **Fig. 3: Results of column experiment for pH (a), alkalinity (b), electrical conductivity (c) and calculated CO$_2$**
255 **saturation (d).**

256 The pH buffering simulated with the suggested mineral assembly agrees well with

257 observations (

258 Fig. 3a). The overestimation of pH during the first few pore volumes can be attributed to the

259 assumed thermodynamic equilibrium with natron. The simulation of electrical conductivity

260 according to solution species mobility matches well the observations (

261 Fig. 3c). Alkalinity (

262 Fig. 3b), which mainly results from carbonate species, was overestimated by the model,

263 possibly due to equilibration with calcite. Despite this, reasonable agreement for CO_2-

264 saturation in the column simulation was achieved (

265 Fig. 3d).

266   Results of the element analysis together with modelled total element concentrations in the

267   column outflow are displayed in Fig. 4.

268   **Fig. 4: Element concentrations (mol l⁻¹) in the column outflow for (a) Na, (b) K, (c) Al and (d) Ca.**

269   The simulation of Na concentrations in Fig. 4a agrees very well with observations.

270   Concentrations of potassium (K) (Fig. 4b) are largely underestimated due to the low

271   solubility of muscovite, which is the only source of K in the chosen mineral model.

272   Aluminium (Al) concentrations in Fig. 4c are overestimated by an order of magnitude

273   compared to measurements. This suggests too high solubility constants for DSP and TCA

274   obtained from the literature or reprecipitation of Al in the form of aluminium oxides such as

275   gibbsite and boehmite or aluminium silicates. The mismatch of Ca concentrations in Fig. 4d

276   together with the overestimated alkalinity from

277   Fig. 3b suggests that calcite may not be present as a pure phase, although it is modelled as

278   such.

279   Overall, the comparison of measured and modelled drainage composition shows that large

280   uncertainties exist in setting key mineralogical properties of residue sand. Despite these

281   shortcomings, the geochemical model is considered suitable for estimating the geochemical

282   evolution of residue sand in field conditions because it is capable of reproducing main

283   geochemical features such as pH, EC and Na concentrations.

284   **3   Hydraulic Model**

285   For the hydraulic characterization of residue sand in variably saturated flow conditions the

286   van Genuchten/Mualem model [54, 55] for water retention and unsaturated hydraulic

287   conductivity as in [56] was used. The van Genuchten function [55] is given by

$$\theta(h) = \begin{cases} \theta_r + \dfrac{\theta_s - \theta_r}{[1 + (\alpha h)^n]^m}, & h < 0 \\ \theta_s, & h \geq 0 \end{cases}, \qquad (3)$$

288 where h is the pressure head (cm), θ is the actual moisture content, θ_r is the residual moisture

289 content, θ_s is the saturated moisture content and α (cm^{-1}), n and $m = 1 - \dfrac{1}{n}$ are soil-specific

290 parameters. The free parameters were determined by fitting Eq. (3) to measurements of water

291 retention that were taken in a pressure range of $0 - 15$ bars using the RETC code [57].

292 Unsaturated hydraulic conductivity according to the Mualem model [54] is given by

$$K(\Theta) = K_s \Theta^l \left[1 - \left(1 - \Theta^{\frac{1}{m}}\right)^m\right]^2, \qquad (4)$$

293 where $\Theta = \dfrac{\theta - \theta_r}{\theta_s - \theta_r}$ is the reduced moisture content. The parameter l was taken as 0.5. The

294 saturated hydraulic conductivity K_s (m d^{-1}) of the residue sand was measured in situ at

295 various depths using a Guelph constant head permeameter. Its value at the soil surface was

296 measured as 12.008 m d^{-1}. Measured values of water retention and the best fit of the van

297 Genuchten function with parameters $\alpha = 0.075$ cm^{-1}, $n = 1.822$, $\theta_s = 0.454$ and $\theta_r =$

298 0.039 are displayed together with unsaturated conductivity in Fig. 5.

299
300 **Fig. 5: Water retention and unsaturated hydraulic conductivity of residue sand at the soil surface according to the van Genuchten/Mualem model.**

301 Conductivity measurements suggest a non-linear relation between K_s and distance to the soil

302 surface z (m) of the form:

$$K_s(z) = a \exp(bz), \qquad (5)$$

303 which was fitted to the data using a least square criterion. The parameters a and b were

304 determined as 12.008 m d^{-1} and -0.885 m^{-1}, respectively, with a coefficient of determination

305 of 0.92.

306   The saturated water content θ_s up to a depth of 3 m was calculated from the measured θ_s at

307   the surface and measured values of dry bulk density (1.3 g cm^{-3} at the surface versus 1.5 g

308   cm^{-3} at 3 m depth). Assuming a constant solid density, a linear relation between depth and

309   θ_s was established according to

$$\theta_s(z) = cz + d, \tag{6}$$

310   with $c = 0.028$ m^{-1} and $d = 0.454$. Depth-dependent measurements of K_s and θ_s together with

311   the fitted Eqs. (5) and (6) are displayed in Fig. 6.

312   **Fig. 6: Depth dependence of saturated hydraulic conductivity K_s (left) and saturated water content θ_s (right).**

313   All other parameters in the van Genuchten/Mualem hydraulic model were assumed constant

314   throughout the profile.

315   Transverse and longitudinal dispersivity in the residue sand were estimated as 10^{-1} m. For

316   simplicity, the influences of water saturation [58, 59] and scale [60] were neglected. The

317   coefficient of molecular diffusion was taken as 3×10^{-10} m^2 s^{-1} according to the PHREEQC

318   default settings (temperature of 25°C).

319   **4   Software for Integrated Hydrogeochemical Modelling**

320   Processes of variably saturated liquid phase flow, multi-component solute transport and

321   geochemical reactions according to the geochemical and hydraulic properties described

322   earlier were combined into an integrated hydrogeochemical model of bauxite residue sand.

323   The employed software results from coupling the multipurpose finite element solver

324   COMSOL [61] with a component object model (COM) version of IPhreeqc. IPhreeqc is a

325   version of the geochemical modelling framework PHREEQC [29] that is specifically

326   designed for coupling to multi-component solute transport simulators [62].

327   **Fig. 7: Program flow and structure.**

328   The main modules of the coupled software and their interactions are illustrated in Fig. 7. The

329   coupling code is executed within the MATLAB scripting environment [63], which contains

330   the split-operator procedure, manages data transfer between the modules and performs pre-

331   and post-processing tasks. From MATLAB, the computation of aqueous phase flow and

332   solute transport for a single time step is directed to the COMSOL module. After updated

333   liquid phase saturations and solute concentrations are transferred back to the MATLAB

334   workspace, the assembly of chemical components that constitutes the liquid phase is sent to

335   IPhreeqc for geochemical speciation using its COM interface. The main advantage over

336   existing couplings of flow and multispecies transport codes with PHREEQC as reaction

337   engine, such as PHTRAN [64], PHT3D [65] and PHWAT [66], results from the fact that

338   IPhreeqc saves in memory the entire geochemical system state between calls to it. Thus, only

339   the information that is relevant to flow and transport computations (liquid phase saturation

340   and element concentrations) needs to be extracted and transferred to COMSOL. In addition,

341   the data transfer is processed entirely in memory, which avoids inefficient writing and

342   reading of data files. A detailed presentation of the software is provided in [67]. Additional

343   features that were specifically implemented for the presented simulations of bauxite residue

344   sand are documented in the Appendices A-C.

345   **5   Meteorological Conditions**

346   In the absence of vegetation, rainfall and evaporation are the driving forces of soil moisture

347   movement and solute transport in the field. Thus, the geochemical evolution of residue sand,

348   the volumes of drainage, and the magnitude of fertiliser leaching, strongly depend on the

349   local meteorological conditions. Daily rainfall and pan evaporation were obtained from

350   ALCOA's meteorological records for the Pinjarra residue storage area (latitude: -32.647036,

351   longitude: 115.930309). Missing values in the evaporation time series were reconstructed by

352   fitting the amplitude and phase of a sine function with wavelength of 365 d to the measured

353   data. The dominance of seasonal fluctuations of evaporation was verified by means of Fourier

354   analysis. Gaps in precipitation records were filled by linear interpolation between

355   measurements. Mean annual precipitation after the reconstruction of missing data amounts to

356   1005 mm. This value agrees well with the 967 mm y^{-1} measured at the town of Pinjarra

357   during the period 1877-1991 [68]. The mean annual value of reconstruction potential

358   evaporation (2400 mm y^{-1}) is considerably higher than the value of 2075 mm y^{-1} from an

359   independent 10-y record (1980-1990) [69]. Nevertheless, the interpolation method for

360   potential evaporation was retained because the influence of evaporation on the overall water

361   balance in the highly conductive sand is limited by water availability in the surface layer. The

362   reconstructed time series of rainfall and potential evaporation at the Pinjarra residue storage

363   site are illustrated in Fig. 8.

364   **Fig. 8: Time series of rainfall and potential evaporation with reconstructed missing values.**

365   In its current form, the model represents bare residue sand prior to or shortly after plant

366   seeding. Therefore, the influence of plants on water availability and water quality is not

367   incorporated in the model. As shown in Wissmeier and Barry [67], however, element-specific

368   root water uptake can be included into the model by using space- and pressure-dependent

369   sink terms in solute transport equations.

370   **6   Simulation of a Field Lysimeter**

371   Currently, no data on fertiliser leaching in residue sand profiles under field conditions are

372   available. At ALCOA's Pinjarra site, however, a field lysimeter has recently been constructed

373   to quantify water and nutrients dynamics in rehabilitated residue sand [70]. In the following,

374   we present a simulation of the geochemical evolution of fertigated and gypsum-amended

375   residue sand in this field lysimeter in response to rainwater leaching under the prevailing

376   meteorological conditions. The simulation period starts with the construction of the lysimeter

377   in August 2007 and ends after 930 d in February 2010.

378   *6.1   Domain, Boundary and Initial Conditions*

379   The lysimeter consists of a 3-m deep pit with vertical walls and a square surface area with

380   sides of 24 m length. The pit is sealed with a high-density plastic liner and drained by

381   regularly spaced (2.5 m spacing) drainage pipes located at 2.8 m below ground level. The

382   domain was simulated as a 2D slice orthogonal to the drainage pipes. Due to symmetry

383   planes halfway between the drainage pipes, at the midpoint of the drainage pipes and at the

384   lateral boundaries, the domain could be reduced to a 1-m wide and 3-m deep column.

385   **Fig. 9: Lysimeter simulation domain and finite element representation.**

386   The simulation domain and its finite element discretization are displayed in Fig. 9. The half

387   circle at $x = 0$ m, $z = -2.8$ m represents part of the drainage pipe where a seepage face

388   boundary according to Eq. (C.1) in Appendix C with $k_{sp} = 10^{-4}$ s^{-1} was applied. At $z = 0$, an

389   atmospheric boundary according to Eq. (C.4) with $H_{crit} = -30$ m, $\xi = 0.4$ s^{-1}, $H_{po} = 0$ m and

390     $k_{po} = 10^{-4}$ s^{-1} was used. A zero-flux condition was employed for the remaining boundaries.

391   The upper part of the domain with predominantly vertical flow was discretized by a

392   quadrilateral mesh with a vertical element size of 3×10^{-3} m at the top boundary. The fine

393   discretization was necessary to capture the sudden changes between infiltration and

394   evaporation in the highly conductive sand. From $z = -2$ m downwards, a triangular mesh with

395   a compressed z-direction and local refinement around the seepage boundary was used. The

396   initial pressure head at the start of the simulation was taken as -1 m. At the top boundary,

397   equilibrium of the infiltrating and evaporating rainwater with atmospheric CO_2 at 3.16×10^{-4}

398   atm and O_2 at 1.99×10^{-1} atm was assumed. The split-operator time step for alternations

399   between flow, transport and reaction calculations was set to 1 d.

400   *6.2   Fertigation and Gypsum Amendment*

401   Further to its natural geochemical properties, residue sand in the 0 – 1.5 m depth interval was

402   amended with gypsum at a rate of 1% by weight. Furthermore, the top 0.2 m of the profile

403   received a one-off addition of 2.7 t/ha of inorganic fertiliser mix mainly comprised of di-

404   ammonium-phosphate (DAP), K_2SO_4 and $MgSO_4$. Phosphate (from DAP) in contact with

405   gypsum is likely to reprecipitate as hydroxyapatite, which is why this mineral was included in

406   the simulations with an initial amount of 0. This is also in agreement with observation in an

407   independent column experiment (data not shown).

408   The amendments were included in the model through additional equilibrium dissolution

409   reactions according to the reaction formulas, equilibrium constants and amounts listed in

410   Table 4.

Table 4: Fertilizer and amendment properties.

Mineral name Reaction formula	Equilibrium constant	Relative amount $(mol\ l_{soil}^{-1})$
Gypsum[a] $CaSO_4{:}2H_2O = Ca^{+2} + SO_4^{-2} + 2\ H_2O$	$10^{-4.61}$ [c]	1.10×10^{-1}
DAP[b] $(NH_4)_2HPO_4 = 2\ NH_4^+ + HPO_4^{-2}$	$10^{0.3}$ [d]	5.67×10^{-3}
Arcanite[b] $K_2SO_4 = SO_4^{-2} + 2\ K^+$	$10^{-1.776}$ [e]	2.41×10^{-3}
MgSO4[b] $MgSO_4 = Mg^{+2} + SO4^{-2}$	$10^{4.8781}$ [f]	1.50×10^{-4}
MnSO4[b] $MnSO_4 = Mn^{+2} + SO_4^{-2}$	$10^{2.669}$ [c]	1.42×10^{-4}
CuSO4[b] $CuSO_4 = Cu^{+2} + SO_4^{-2}$	$10^{3.01}$ [c]	1.55×10^{-4}
Zincosite[b] $ZnSO_4 = Zn^{+2} + SO_4^{-2}$	$10^{3.01}$ [c]	1.11×10^{-3}
Borax[b] $Na_2(B_4O_5(OH)_4){:}8H_2O + 2\ H^+ = 4\ B(OH)_3 + 2\ Na^+ + 5\ H_2O$	$10^{12.464}$ [e]	2.62×10^{-5}
Hydroxyapatite $Ca_5(PO_4)_3OH + 4\ H^+ = H_2O + 3\ HPO_4^{-2} + 5\ Ca^{+2}$	$10^{-3.421}$ [g]	0.00

[a] applied to the top 1.5 m, [b] applied to the top 0.2 m, [c] minteq.dat, [d] calculated from solubility in pure water [71], [e] pfitzer.dat, [f] llnl.dat, [g] phreeqc.dat

As can be seen from Eq. (1), the rate of concentration changes due to the kinetic dissolution

of TCA and sodalite is dependent on the ratio of reactive surface to solution volume. In

unsaturated residue sand with an average moisture content of 0.2, this ratio is approximately

40 times larger than in the acid neutralization experiment. Therefore, the assumption of local

thermodynamic equilibrium was extended to TCA and sodalite.

419   *6.3   Results and Discussion*

420   *6.3.1   Dynamic Water Balance*

421   Results of the dynamic water balance for the simulation period of 930 d starting on 1 August

422   2007 are displayed in . The surface flux in (Fig. 10a) was normalized by the infiltrating area

423   and reflects the strong events during winter, which were immediately followed by marked

424   evaporation. Despite high potential evaporation during summer, actual evaporation was

425   effectively shut down due to the limited water availability in the upper soil profile. Discharge

426   in Fig. 10b was also normalized with respect to the infiltrating area for better comparability.

427   The water infiltrated during the 2007 rainfall season at the beginning of the simulation

428   reaches the drainage pipe after 60 d. Before any discharge is produced, the domain below the

429   drainage pipe was saturated. The initial filling of the lysimeter bottom during the first 60 d

430   can be followed in the evolution of average moisture contents (Fig. 10c). The fast discharge

431   recession leads to very low outflow rates during summer months. Despite the fully saturated

432   lysimeter bottom, the moisture content frequently declined below a domain average of 0.15

433   during summers. This is also confirmed experimentally by in-situ moisture probes and

434   neutron probe measurements.

435   **Fig. 10: Dynamic water balance of lysimeter simulation with (a) surface flux (mm d⁻¹), (b) drainage at the drainage**
436   **pipe (mm d⁻¹) and (c) average soil moisture content θ.**

437   Overall, the simulation of soil moisture in the lysimeter (Fig. 10) indicates very dry

438   conditions throughout the entire simulation period. During summers, the water content

439   frequently decreased to values close to the residual (i.e., plant-unavailable) moisture content

440   in the upper metre of the profile. Despite low moisture contents, the average fluid pressure

441   did not drop below the permanent wilting point (PWP: $h = -15$ bar). However, near the

442   surface the PWP was frequently reached. In addition, the sand contains only marginally more

443   water at -1 bar than at -15 m due to the steep gradient of water retention $\frac{dh}{d\theta}$ (Fig. 5). Even

444 during rainfall seasons, the moisture content hardly exceeded 0.2 in the upper 2.5 m of the

445 domain. Despite the poor water holding capacity of the sand, only about 46% of the total

446 rainfall left the lysimeter as drainage. The rest was lost by evaporation or stored in the

447 initially dry profile. Thus, the water supply alone imposed conditions that were challenging,

448 but not inhibiting, for plant growth in the lysimeter.

449 *6.3.2   Solution Chemistry*

450 Fig. 11 illustrates the evolution of vertical profiles of moisture content, pH and selected

451 solution element concentrations at the right domain boundary ($x = 1$ m). Despite the local

452 outflow at the drainage pipe ($x = 0$ m), only minor lateral variations of geochemistry and

453 moisture conditions were observed. Moisture content profiles show the development of the

454 groundwater table below the drainage pipe as response to the winter rainfall around 50 d. The

455 upper part of the soil column then dried out over summer until the beginning of the following

456 rainy season. The pH profiles show a fast reduction of pH in the upper soil profile to about 11

457 from an initial value of 12.5 caused by gypsum dissolution and calcite precipitation. In the

458 lower profile below -1.5 m, the pH was governed by dissolved natron.

459 **Fig. 11: Evolution of moisture content, pH and concentration of selected elements at the right domain boundary of**
460 **the lysimeter simulation.**

461 With the second winter's rainfall starting at around 300 d, the pH reduced to values around

462 10 in the upper soil profile and with the third winter's rainfall in the entire profile. The

463 initially high Na concentration from natron dissolution was flushed into the lower part of the

464 domain with the first rainfall. The second rainfall period almost completely removed Na from

465 the system, due to the comparatively low solubility of sodalite and analcime. Carbon, as

466 carbonate (CO_3^{-2}) from natron dissolution, immediately reprecipitated as calcite in the upper

467 part of the domain due to the large supply of Ca from gypsum dissolution. The remaining

468 carbon in the un-amended region of the domain was removed after approximately 50 d. Ca

24

469 concentrations show a complex pattern mainly governed by the solubility of calcite and

470 gypsum, both of which are controlled by pH. The decrease in Ca at the top boundary during

471 the second and third rainfall period indicates complete removal of gypsum, which was not

472 observed in the field. This is most likely due to non-equilibrium of gypsum with the soil

473 solution as result of inhomogeneous amendment of the gypsum. During the following

474 evaporation events, the upwards flowing solution was concentrated due to the removal of

475 H_2O at the surface. However, evaporation essentially stops during the dry season because of

476 low moisture contents at the surface. Sulphur, as sulphate (SO_4^{-2}), behaved similarly to Na in

477 the region of gypsum amendment above -1.5 m. Its high initial concentration, resulting from

478 the equilibrium between gypsum and calcite, was flushed almost entirely within the first 300

479 d. Nitrogen (N(-3) as sum of NH_4^+ and NH_3) was decoupled from oxidized forms (e.g., NO_3^-)

480 to avoid instantaneous conversion to N(+5). N(-3) concentrations are displayed representative

481 for the fertilizer elements copper (Cu), zinc (Zn) and boron (B), which show very similar

482 concentration patterns. Their concentration ranges correspond to the amounts of the applied

483 fertilizer minerals (Table 4). The fertilizer elements were carried downwards through the soil

484 profile with the first winter rainfall, and with the second winter's rainfall, they were flushed

485 from the profile without significant retention. Due to high Ca concentrations the model

486 predicted reprecipitation of hydroxyapatite ($Ca_5(PO_4)_3OH$), which retains phosphate (P) in

487 the profile. K concentrations were significantly retarded compared to nitrogen because of

488 temporary adsorption on the cation exchange sites. Magnesium (Mg) shows a mixture of the

489 conservative transport pattern of nitrogen and the exchange pattern of K. High initial Al

490 concentrations in the lower half of the domain resulted from the dissolution of TCA, which is

491 enhanced by reprecipitation of Ca as calcite. In the gypsum-amended part of the soil, TCA

492 dissolution was inhibited by gypsum dissolution. Silica (Si) shows the same concentration

493   pattern as chloride. Both elements were controlled by the dissolution of sodalite, which was

494   activated after the complete removal of TCA.

495   *6.3.3   Minerals*

496   Fig. 12 illustrates the evolution of the main mineral phases in residue sand. Muscovite and

497   analcime did not show any significant response towards leaching during the simulation period

498   and so are omitted in the figure. The other residue minerals show only minor changes in the

499   upper few decimetres of the domain. Gypsum was removed from the top 0.5 m after 3 y of

500   rainfall. However, due to the equilibrium assumption, a considerable amount of gypsum in

501   the top 1.5 m instantaneously transformed into calcite, taking up most of the CO_3^{-2} from

502   natron dissolution. Apart from this increase, calcite shows little response to leaching. Almost

503   half of the initial amount of TCA was immediately dissolved in the untreated residue sand

504   where Ca re-precipitated to calcite with the CO_3^{-2} from natron dissolution. This

505   transformation was suppressed by gypsum in the in the upper part of the domain. However,

506   the fertilizers in the top 0.2 m enhanced TCA dissolution. Leaching of the third rainfall

507   season around 700 d removed TCA from the top 0.2 m. Sodalite shows no reaction towards

508   gypsum and fertilizer amendment. It was slowly leached from the first few centimetres of the

509   soil profile during the three simulated rain seasons once TCA and gypsum were removed.

510   **Fig. 12: Evolution of the main minerals at the right domain boundary of the lysimeter simulation.**

511   *6.3.4   Cation Exchange*

512   The evolution of the exchange species is illustrated in Fig. 13. The initial exchanger

513   composition was dominated by Na, which was replaced mainly by Ca during the course of

514   the simulation. Al is omitted in the figure due to insignificant adsorption in the high pH

515   environment, where it was mainly present in anionic form as $Al(OH)_4^-$. At the transition from

516   the Na to Ca-dominated exchanger, adsorption of K, N(-3), Mg and Mn took place. Despite

517 the higher affinity of standard exchangers for divalent ions, K was the most adsorbed

518 fertilizer element. This is because of its higher concentration compared to divalent fertilizer

519 elements and its large affinity relative to other monovalent fertilizer elements. N(-3) as NH_4^+,

520 which was retained in the upper part of the profile during the first summer, was almost

521 completely removed during the second rainfall period. The low adsorption of N(-3) resulted

522 from its speciation into uncharged NH_3 at pH values above 9. The amount of adsorbed Mg,

523 which is representative for the adsorption pattern of Mn (maximum adsorbed amount 1.5 ×

524 10^{-5} mol l_{soil}^{-1}), increased after 400 d. The adsorption of zinc and copper was insignificant due

525 to low solution concentrations (maximum adsorbed amounts 10^{-8} mol l_{soil}^{-1} and 3 × 10^{-11} mol

526 l_{soil}^{-1}, respectively).

527 **Fig. 13: Evolution of the exchanger composition at the right domain boundary of the lysimeter simulation.**

528 Overall, the predicted geochemical conditions in the lysimeter were still unfavourable for

529 plant growth after 3 y, both in terms of water availability and quality. Even though the main

530 soluble ions Na^+ and SO_4^{-2} were flushed from the system, a pH of 10 was maintained. The

531 plant nutrient status was not sustainably improved by fertilizer amendment. Only K was

532 significantly retained by initially Na-filled adsorption sites. Adsorption of other fertilizer

533 cations including NH_4^+ was insignificant due to (i) their low concentrations compared to the

534 major solutions ions Na and Ca, (ii) their speciation into neutral or negatively charged ions at

535 high pH, and (iii) the low exchange capacity of residue sand. The chromatographic sequence

536 from a Na-dominated exchanger through the temporary adsorption of fertilizer cations to a

537 Ca-dominated system can be interpreted as a snowplough [72-74]. The buffering minerals,

538 TCA, sodalite and calcite that stabilize the pH around 10 were removed from the top few

539 centimetres of the profile. As intended by the gypsum amendment, solution alkalinity was

540 converted to calcite [75, 76]. This procedure, however, did not remove the alkalinity from the

541 system converted it into solid form and prevents the removal of TCA [77].

7 Simulation of Surface Cover for Storage Facilities

542

543 In order to evaluate the performance of fertigated and gypsum-amended residue sand as a

544 surface cover for storage facilities, the hydrogeochemical model was applied to a stratum of

545 sand overlaying low permeability residue mud. Apart from the domain geometry and

546 discretization, the hydrological and geochemical conditions of the lysimeter simulation were

547 adopted including fertigation and gypsum amendment. In contrast to the lysimeter with

548 predominantly vertical flow, the development of a water table at the border to the residue

549 mud introduces a considerable horizontal flow component.

550 *7.1 Domain, Boundary and Initial Conditions*

551 The simulation represents a 3-m thick by 100-m wide layer of residue sand on top of a

552 storage impoundment. Due to symmetry across the centre line, the actual simulation domain

553 was confined to a slice of the cover layer from $x = 0$ m to $x = 50$ m with a symmetry

554 boundary at the right hand side border of the domain. The domain was represented by 10,829

555 computational nodes. For enhanced lateral drainage, the cover layer was conceptualized with

556 a slope of 1.74%. Water losses at the interface to the residue mud at the domain bottom were

557 approximated by a constant flux of 8.3×10^{-7} m s^{-1} in water-saturated conditions and zero

558 flux otherwise. The magnitude of this deep percolation was taken as the saturated hydraulic

559 conductivity of red mud [3], in which case the flux corresponds to gravity-driven drainage.

560 The left hand side of the domain was represented by a seepage face boundary according to

561 Eq. (C.1) with a stiff-spring constant of $k_{sp} = 10^{-3}$ s^{-1}. Atmospheric forcing of the system was

562 imposed via an atmospheric boundary condition at the top of the domain. In order to predict

563 the evolution of the sand cover for 5 y, the measured meteorological time series of 3 y were

564 repeatedly applied to the soil surface.

7.2   Results and Discussion

7.2.1   Dynamic Water Balance

The dynamic water balance of the surface cover simulation is illustrated in Fig. 14. For better

comparability with the lysimeter simulation (Fig. 10), the *y*-axis scaling was retained.

Compared to the lysimeter simulation the surface cover exhibits much larger water storage

capacity and slower recession of discharge during dry periods due to impeded drainage (Fig.

14b). As in Fig. 10, the drainage flux was normalized to the inflow area for comparability. At

the beginning of the simulation period, a perched water table evolved at the border to the

low-permeability mud. Due to this water table, the average soil moisture (Fig. 14c) was at

much higher levels (0.2-0.3) compared to the lysimeter simulation.

Fig. 14: Dynamic water balance of surface cover simulation, with (a) surface flux (mm d^{-1}), (b) drainage (mm d^{-1}) and (c) average soil moisture content θ.

7.2.2   Solution Chemistry

Time-dependent profiles of normalized soil moisture, $\Theta = \frac{\theta - \theta_r}{\theta_s - \theta_r}$, selected total element

concentrations and pH are displayed in Fig. 15 with different scales for the *x*- and *y*-axes.

Different colour scales were used for the plots from 1 to 50 d and from 400 to 1825 d because

the low fertilizer concentrations after the first rainfall period would otherwise be

indistinguishable in the later profiles. Display times were selected during the first rainfall

period (1-50 d), in the middle of the second rainfall period (400 d), after the third rainfall

period (1000 d) and at the end of 5 y of atmospheric leaching (1825 d).

Normalized water contents illustrate the build-up of soil moisture at the border of the residue

mud and the evolution of a perched water table. The results at 400 and 1000 d show water

table fluctuations from winter to summer.

588 **Fig. 15: Evolution of normalized moisture content, concentrations of selected elements and pH profiles of the surface**
589 **cover simulation at 1, 20, 50, 400, 600 and 1825 d.**

590 Until the last profile at 1825 d, Ca that mainly originates from gypsum and TCA dissolution

591 did not enter the saturated zone. Declining concentrations at the top of the domain indicate

592 complete removal of gypsum and TCA. Na was flushed from the unsaturated zone with the

593 first rainfall event. Due to the velocity field in the saturated groundwater lens, concentrations

594 were more persistent towards the right hand side of the domain. However, after the third

595 rainfall season (1000 d) most of the Na has been removed. N(-3) is representative for all

596 fertilizer elements besides K. Through dilution and dispersion, concentrations decreased with

597 the first infiltration water. During the second rainfall period around 400 d, the fertilizers were

598 removed from the unsaturated zone. However, they remained in the groundwater lens at

599 roughly a tenth of their original concentration. Fertilizer concentrations decreased further

600 during the third rainfall season until they were removed completely after 5 y of leaching. The

601 behaviour of K, the most adsorbing element, was very similar to N(-3). As result of the

602 exchange process, however, its removal was delayed compared to the other fertilizer

603 elements. During the first rainfall period, the pH behaved similarly to the lysimeter

604 simulation because of essentially 1D flow. After the perched water table has established, two

605 pH regions were separated by the line of the groundwater table in moist conditions. The pH

606 in the saturated region was persistent until it was eventually leached to pore water levels in

607 the unsaturated zone after 5 y. In the profiles at 1000 and 1825 d the removal of gypsum and

608 TCA at the top of the domain decreased the pH to around 9.

609 *7.2.3   Minerals*

610 The evolution of the main minerals in the surface cover is illustrated in Fig. 16. During 5 y of

611 rainfall, gypsum was removed from the top metre of the profile. In this zone, calcite showed

612 hardly any response to leaching. However, additional precipitation was predicted at the lower

30

613   boundary of the gypsum-amended region and in the saturated zone. TCA was removed from

614   the top 0.5 m and from the saturated zone, while sodalite was only removed from the top few

615   decimetres. Exchange processes are dominated by Na-Ca exchange, and are omitted since the

616   results are similar to those for the lysimeter.

617   In summary, the results show that water availability was improved in the surface cover by the

618   formation of a perched groundwater table. Waterlogged conditions with evaporation-induced

619   salt accumulation at the soil surface [78-80] were avoided by the slope of the underlying low-

620   permeability mud and lateral drainage. Due to its large water volume, the saturated zone

621   acted as a buffer for infiltrating solutes and retained fertilizer ions. However, enhanced water

622   retention also retained adverse soil properties such as high pH and Na concentrations, which

623   decreased the efficiency of natural leaching.

624   **Fig. 16: Evolution of the main minerals of the surface cover simulation for 1 and 1825 d.**

625   **8   General Discussion**

626   *8.1   Model Uncertainties*

627   The model for mineral reactions in bauxite residue sand comprises large uncertainties, even

628   though all components of the mineral assembly have been previously identified in residue of

629   different origins [30, 34, 41, 81]. The mineral assembly as deduced from acid neutralization

630   alone is not unique and other combinations of minerals may reproduce pH buffering equally

631   well. Sodalite and additional amounts of natron, for instance, yield excellent agreement with

632   acid neutralization at 96 h. However, this would require the kinetic dissolution of natron at a

633   timescale of days, which is not plausible unless it is partially occluded within the profile. In

634   order to increase the reliability of the predictions, detailed quantification of the reactive

635   minerals specifically for Pinjarra residue sand would be required. Furthermore, equilibrium

636   constants vary widely among authors and databases, particularly for different forms of

637   tricalcium aluminates but also for muscovite and analcime. Measurements of the

638   stoichiometry and solubility of reactive minerals on phases isolated from the residue would

639   be desirable. This is also important because most reactive minerals form during the refining

640   process, so that their reactivity and stoichiometry depends on the bauxite source and

641   processing conditions [32, 33, 39, 82, 83]. The fact that Khaitan et al. [34] attribute the pH

642   buffering capacity of residue from Jamaican bauxite mainly to TCA and calcite whereas

643   Menzies et al. [41] and Snars and Gilkes [30] hold mainly sodalite and calcite responsible for

644   pH control indicates the large uncertainty in the recent literature. In the mineral assembly

645   determined in this study, both phases contribute to pH buffering in roughly equal parts.

646   Acknowledging the large uncertainties, the derived mineral composition can be regarded as a

647   surrogate for major geochemical properties such as pH, electrical conductivity and Na

648   concentrations. Concentrations of elements that are not components of an included mineral,

649   such as iron, Mg and titanium (Ti), cannot be predicted.

650   In a recent study, Phillips and Chen [14] found a large contribution (8-12 cmol kg_{solid}^{-1}) of

651   pH-dependent variable charge adsorption sites to the overall adsorption characteristics of

652   residue sand. Menzies et al. [41] measured the effective exchange capacity of seawater

653   neutralized residue sand as 18.6 cmol kg_{solid}^{-1} from which they attributed 6 cmol kg_{solid}^{-1} to

654   variable charge. These values exceed the cation exchange capacity measured in this study by

655   a factor of 10-20. However, both previous studies rely on compulsive exchange of K^+ with

656   NH_4^+. As shown in Fig. 4b, considerable amounts of K are released by mineral dissolution.

657   Therefore, K concentrations cannot be considered to result solely from exchange processes,

658   which may lead to an overestimation of the effective exchange capacity. The presumed pH-

659   dependency of the exchange sites may in fact reflect the solubility of the source mineral (e.g.,

660   muscovite). On the other hand, the effective exchange capacity in our study may have been

661 reduced by the washing procedure, particularly through the removal of surface aluminous and

662 ferric oxides that contribute to variable charge adsorption sites. Nevertheless, we employ the

663 lower value of cation exchange capacity on washed residue since it gives a more conservative

664 estimate of nutrient retention. Because pH levels during the simulations were well above the

665 point of zero charge of ferrous and aluminous oxides [84, 85], charge characteristics are not

666 expected to change significantly. This justifies the use of a simple exchange model for

667 adsorption. However, the adsorption behaviour of cations onto zeolites such as sodalite is

668 influenced by the window size of their cage structure [86-90]. Thus, the applicability of

669 standard affinity constants for the simulation of cation exchange remains uncertain [91].

670 The dynamic water balance is regarded as relatively reliable since the parameters for soil

671 moisture movement are directly measured or derived from measurements according to

672 standard procedures (e.g., water retention).

673 An obvious weakness of the simulations is the lack of in-depth model validation due to the

674 scarcity of analytical data.

675 *8.2   Implications for Bauxite Residue Management*

676 Despite the model uncertainties, the main results are plausible and consistent with

677 observations. Because the model is adapted to the geochemical and meteorological conditions

678 at the Pinjarra refinery, findings are site-specific but can be generalized to residue sand with

679 similar properties and in comparable climatic conditions.

680 The lysimeter simulation illustrates the poor water retention in the residue sand with low

681 plant-available soil moisture content. Thus in well-drained systems water availability is a

682 limiting factor for plant growth. The simulation of the cover layer shows that the moisture

683 status in residue sand can be improved by the appropriate design of the horizontal distance

684   between drains, the thickness of the cover layer and its slope. If these parameters are not

685   chosen carefully, for example if the distance between drains is too large, waterlogged

686   conditions with adverse effects on plant growth may result (simulation results not shown).

687   The development of a shallow water table increases evaporation losses during the summer

688   months. Although not observed in our simulations, this may lead to salt accumulation at the

689   soil surface [e.g., 78, 79]. The amendment of residue sand with fine-textured residue mud

690   would improve the soil water retention but at the same time worsens the geochemical

691   properties through enhanced pH buffering [92]. Compared to the hydrological situation, the

692   geochemical properties of the residue sand are seen as more severe constraints for plant

693   growth. Mineral reactions in amended fresh residue sand are governed by the initial

694   dissolution of natron and gypsum, where Ca and CO_3^{-2} precipitate as calcite while the soluble

695   $Na_2SO_4^{-2}$ is flushed. Even though gypsum amendment reduces the solution pH to 10, leaching

696   of TCA and therefore the sustainable decrease of pH buffering in the sand is inhibited. From

697   the main buffering minerals, TCA and sodalite are very resistant to rainwater leaching due to

698   their low solubility. Efficient retention of fertilizers is prevented by (i) the low cation

699   exchange capacity of residue sand, (ii) competition with high levels of Ca and Na for

700   exchange sites, and (iii) the speciation of fertilizer elements into uncharged or negative ions

701   at elevated pH (e.g., NH_3). Therefore, the addition of fertilizers to gypsum-amended fresh

702   residue sand only temporarily improves the plant nutrient status. Natural attenuation of

703   gypsum-amended and fertigated residue sand through atmospheric leaching is not a viable

704   long-term option to improve the hydrogeochemical properties for establishing a sustainable

705   vegetation cover.

706   Instead, we propose a comprehensive treatment scheme that aims at improving all major

707   aspects of soil fertility:

708   1. Removal of most soluble mineral fractions – e.g., through seawater neutralization [5, 41, 93, 94] – to decrease the solid pH buffering capacity and attenuate the competition with fertilizer ions for exchange sites;

711   2. Amendment with a fine textured mineral soil (not residue mud) to improve water retention and cation exchange capacity;

713   3. Adaption of surface cover dimensions to the hydraulic properties of the substrate with regularly spaced drains to improve the water balance;

715   4. Amendment with organic fertilizer to establish a natural microbial community, increase the adsorption capacity [6, 8, 95-97]; and

717   5. Application of inorganic fertilizers [10, 12, 16, 17, 95, 98] to improve the plant nutrient status.

719 **9   Conclusions**

720 We present the application of a software coupling of COMSOL and IPhreeqc for interactions

721 of comprehensive geochemical reactions and 2D variably saturated soil moisture movement

722 to evaluate the environmental behaviour of bauxite refining residue sand. The main findings

723 of the simulations are:

724   • In well-drained residue sand, the average moisture content drops below 0.1 for extended periods during summer, which poses limitations to plant growth.

726   • By adapting the dimensions and drainage of residue storage facilities to the hydraulic properties of the cover material (e.g., mixtures of sand and clay), a plant-suitable moisture content can be maintained also during the dry summer months.

729   • Nonrecurring fertilizer application on fresh residue sand does not alter the long-term plant nutrient status due to low cation exchange capacity, competition with predominant solution ions and speciation into neutral or negative form.

732   •   Gypsum amendment ameliorates the pH to around 10 but suppresses the dissolution

733   of TCA and therefore hampers the sustainable leaching of solid alkalinity.

734   Thus, we conclude that gypsum-amendment and application of inorganic fertilizers alone

735   does not sufficiently improve the geochemical conditions in residue sand to promote a

736   vigorous and sustainable vegetation cover. Since the minerals in residue sand have a very

737   high buffering capacity and annual recharge rates in southwest Western Australia are low,

738   natural attenuation of the sand's pH via rainfall leaching is predicted to be in the order of tens

739   of years. For the successful revegetation of residue storage facilities all aspects of soil fertility

740   need to be addressed before residue sand can serve as valuable medium for plant growth. A

741   logical step for future model development would be the incorporation of biological

742   transformations by plants and soil microbes.

747   **References**

748   [1]   IAI International Aluminium Institute, 2011. Alumina production, Available from:
749   http://world-aluminium.org/?pg=statistics, accessed 15.04.2011.

750   [2]   CSIRO, 2011. Bauxite residue database, Available from:
751   http://www.csiro.au/products/Bauxite-residue-database.html, accessed 15.04.2011.

752   [3]   J.B. Wehr, I. Fulton, N.W. Menzies, Revegetation strategies for bauxite refinery
753   residue: A case study of Alcan Gove in Northern Territory, Australia, Environ
754   Manage, 37 (2006) 297-306.

755 [4] ALCOA World Alumina, 2011. Dry stacking of bauxite residue, Available from:
756   http://www.alcoa.com/global/en/environment/pdf/Dry_Stacking_Case_Study1.pdf,
757   accessed 15.04.2011.

758 [5] G. Power, M. Gräfe, C. Klauber, 2009. Review of current bauxite residue
759   management, disposal and storage: Practises, engineering and science. CSIRO.

760 [6] R.G. Courtney, S.N. Jordan, T. Harrington, Physico-chemical changes in bauxite
761   residue following application of spent mushroom compost and gypsum, Land
762   Degradation & Development, 20 (2009) 572-581.

763 [7] R.G. Courtney, J.P. Timpson, Reclamation of fine fraction bauxite processing residue
764   (red mud) amended with coarse fraction residue and gypsum, Water, Air, and Soil
765   Pollution, 164 (2004) 91-102.

766 [8] R.G. Courtney, J.P. Timpson, Nutrient status of vegetation grown in alkaline bauxite
767   processing residue amended with gypsum and thermally dried sewage sludge - A two
768   year field study, Plant and Soil, 266 (2004) 187-194.

769 [9] L.R. Hossner, R.H. Loeppert, 1984. Reclamation and vegetation of bauxite residue,
770   Project Report to Aluminum Company of America. Soil & Crop Science Department
771   Texas A&M University: Point Comfort, Texas.

772 [10] C. Thiyagarajan, I.R. Phillips, B. Dell, R.W. Bell, Micronutrient fractionation and
773   plant availability in bauxite-processing residue sand, Australian Journal of Soil
774   Research, 47 (2009) 518-528.

775 [11] H.J. Woodard, L. Hossner, J. Bush, Ameliorating caustic properties of aluminum
776   extraction residue to establish a vegetative cover, Journal of Environmental Science
777   and Health - Part A Toxic/Hazardous Substances and Environmental Engineering, 43
778   (2008) 1157-1166.

779 [12] R. Courtney, G. Mullen, T. Harrington, An evaluation of revegetation success on
780   bauxite residue, Restoration Ecology, 17 (2009) 350-358.

781 [13] M.J. Gherardi, Z. Rengel, Bauxite residue sand has the capacity to rapidly decrease
782   availability of added manganese, Plant and Soil, 234 (2001) 143-151.

783 [14] I.R. Phillips, C. Chen, Surface charge characteristics and sorption properties of
784   bauxite-processing residue sand, Australian Journal of Soil Research, 48 (2010) 77-
785   87.

786 [15] B.E.H. Jones, R.J. Haynes, Bauxite Processing Residue: A Critical Review of Its
787   Formation, Properties, Storage, and Revegetation, Critical Reviews in Environmental
788   Science and Technology, 41 (2011) 271-315.

789 [16] C.R. Chen, I.R. Phillips, L.L. Wei, Z.H. Xu, Behaviour and dynamics of di-
790   ammonium phosphate in bauxite processing residue sand in Western Australia-II.
791   Phosphorus fractions and availability, Environmental Science and Pollution Research,
792   (2009) 1-9.

793 [17] C.R. Chen, I.R. Phillips, L.L. Wei, Z.H. Xu, Behaviour and dynamics of di-
794   ammonium phosphate in bauxite processing residue sand in Western Australia-I. NH3

795   volatilisation and residual nitrogen availability, Environmental Science and Pollution
796   Research, (2009) 1-12.

797   [18]   P.C. Lichtner, Continuum model for simultaneous chemical-reactions and mass-
798   transport in hydrothermal systems, Geochim Cosmochim Ac, 49 (1985) 779-800.

799   [19]   P.C. Lichtner, Continuum formulation of multicomponent-multiphase reactive
800   transport, in: P.C. Lichtner, C.I. Steefel, E.H. Oelkers (Eds.) Reactive Transport in
801   Porous Media, Mineralogical Society of America, Washington DC, 1996, pp. 1-81.

802   [20]   C.I. Steefel, New directions in hydrogeochemical transport modeling: Incorporating
803   multiple kinetic and equilibrium reaction pathways, in: L.R. Bentley, J.F. Sykes, C.A.
804   Brebbia, W.G. Gray, G.F. Pinder (Eds.) Computational Methods in Water Resources,
805   Balkema, Rotterdam, 2000, pp. 331-338.

806   [21]   C.I. Steefel, D.J. DePaolo, P.C. Lichtner, Reactive transport modeling: An essential
807   tool and a new research approach for the Earth sciences, Earth Planet Sc Lett, 240
808   (2005) 539-558.

809   [22]   B. Hanson, J.W. Hopmans, J. Šimůnek, Leaching with subsurface drip irrigation
810   under saline, shallow groundwater conditions, Vadose Zone Journal, 7 (2008) 810-
811   818.

812   [23]   B.R. Hanson, J. Šimůnek, J.W. Hopmans, Evaluation of urea-ammonium-nitrate
813   fertigation with drip irrigation using numerical modeling, Agricultural Water
814   Management, 86 (2006) 102-113.

815   [24]   A.I. Gärdenäs, J.W. Hopmans, B.R. Hanson, J. Šimůnek, Two-dimensional modeling
816   of nitrate leaching for various fertigation scenarios under micro-irrigation,
817   Agricultural Water Management, 74 (2005) 219-242.

818   [25]   J. Šimůnek, D. Jacques, M.T. van Genuchten, D. Mallants, Multicomponent
819   geochemical transport modeling using HYDRUS-1D and HP1, Journal of the
820   American Water Resources Association, 42 (2006) 1537-1547.

821   [26]   J. Šimůnek, S.A. Bradford, Vadose zone modeling: Introduction and importance,
822   Vadose Zone Journal, 7 (2008) 581-586.

823   [27]   L. Wissmeier, D.A. Barry, Reactive transport in unsaturated soil: Comprehensive
824   modelling of the dynamic spatial and temporal mass balance of water and chemical
825   components, Advances in Water Resources, 31 (2008) 858-875.

826   [28]   L. Wissmeier, A. Brovelli, C. Robinson, F. Stagnitti, D.A. Barry, Pollutant fate and
827   transport in the subsurface, in: Modelling of Pollutants in Complex Environmental
828   Systems, ILM Publications, 2009, pp. 99-143.

829   [29]   D.L. Parkhurst, C.A.J. Appelo, 1999. User's guide to PHREEQC (version 2): A
830   computer program for speciation, batch-reaction, one-dimensional transport, and
831   inverse geochemical calculations. U.S. Geological Survey: Denver, Colorado.

832   [30]   K. Snars, R.J. Gilkes, Evaluation of bauxite residues (red muds) of different origins
833   for environmental applications, Applied Clay Science, 46 (2009) 13-20.

834 [31] S. Taylor, N. Pearson, 2001. Properties of Bayer process solids from Alcoa WA
835 refineries and their component minerals. ALCOA World Alumina: Technology
836 Delivery, Internal Report.

837 [32] B.I. Whittington, T.M. Fallows, M.J. Willing, Tricalcium aluminate hexahydrate
838 (TCA) filter aid in the Bayer industry: factors affecting TCA preparation and
839 morphology, International Journal of Mineral Processing, 49 (1997) 1-29.

840 [33] B.I. Whittington, C.M. Cardile, The chemistry of tricalcium aluminate hexahydrate
841 relating to the Bayer industry, International Journal of Mineral Processing, 48 (1996)
842 21-38.

843 [34] S. Khaitan, D.A. Dzombak, G.V. Lowry, Chemistry of the acid neutralization
844 capacity of bauxite residue, Environmental Engineering Science, 26 (2009) 873-881.

845 [35] G.E. Ho, W.A. Robertson, G.I. Roach, A. Antonovsky, Morphological study of bayer
846 process desilication product and its application to laboratory and plant digests,
847 Industrial & Engineering Chemistry Research, 31 (1992) 982-986.

848 [36] J.L. Lowe, R.D. Hart, P.G. Smith, A.L. Rohl, G.M. Parkinson, Morphology and
849 crystllinity: Insight into the mechanism of growth of DSP, in: 7th International
850 Alumina Quality Workshop, CSIRO Minerals, Waterford, WA, Western Australia,
851 2005, pp. 168-173.

852 [37] T. Picaro, B. Pei, A.R. Kane, M.R. Thornber, A.B. Fletcher, Separation and
853 mineralogical analysis of bayer red mud, Developments in Chemical Engineering and
854 Mineral Processing, 10 (2002) 475-489.

855 [38] P.G. Smith, R. Pennifold, T. Lwin, A. Kane, The composition of DSP formed under
856 predesilication and high temperature Bayer digestion conditions, in: Light Metals:
857 Proceedings of Sessions, TMS Annual Meeting (Warrendale, Pennsylvania), 2001,
858 pp. 5-11.

859 [39] B. Whittington, T. Fallows, Formation of lime-containing desilication product (DSP)
860 in the Bayer process: factors influencing the laboratory modelling of DSP formation,
861 Hydrometallurgy, 45 (1997) 289-303.

862 [40] B.I. Whittington, B.L. Fletcher, C. Talbot, The effect of reaction conditions on the
863 composition of desilication product (DSP) formed under simulated Bayer conditions,
864 Hydrometallurgy, 49 (1998) 1-22.

865 [41] N.W. Menzies, I.M. Fulton, R.A. Kopittke, P.M. Kopittke, Fresh water leaching of
866 alkaline bauxite residue after sea water neutralization, Journal of Environmental
867 Quality, 38 (2009) 2050-2057.

868 [42] W. Stumm, J.J. Morgan, Aquatic Chemistry: Chemical Equilibria and Rates, Wiley,
869 New York, 1996.

870 [43] J. Doherty, 2004. PEST model-independent parameter estimation, User manual: 5th
871 edition. Watermark Numerical Computing: Australia.

872 [44] M.R. Thornber, C.A. Hughes, The alkalinity of residues from Alcoa of Australia
873 Limited's refineries of south-west Australia, in: International Bauxite Tailings

874 Workshop, Executive Management Services, Perth Western Australia, 1992, pp. 136-
875 147.

876 [45] J. Schott, O.S. Pokrovsky, E.H. Oelkers, The link between mineral
877 dissolution/precipitation kinetics and solution chemistry, in: E.H. Oelkers, J. Schott
878 (Eds.) 19th Annual V M Goldschmidt Conference, Mineralogical Soc Amer, Davos,
879 Switzerland, 2009, pp. 207-258.

880 [46] N. Komada, E.F. Westrum, B.S. Hemingway, M.Y. Zolotov, Y.V. Semenov, I.L.
881 Khodakovsky, L.M. Anovitz, Thermodynamic properties of sodalite at temperatures
882 from 15 K to 1000 K, Journal of Chemical Thermodynamics, 27 (1995) 1119-1132.

883 [47] R.L. Cooley, R.L. Naff, Regression modeling of ground-water flow, in: U.S.
884 Geological Survey open-file report USGS-TWRI Book 3 Chapter B4, USGS Denver,
885 CO, 1990, pp. 85-180.

886 [48] C. Amrhein, D.L. Suarez, Procedure for determining sodium-calcium selectivity in
887 calcareous and gypsiferous soils, Soil Science Society of America Journal, 54 (1990)
888 999-1007.

889 [49] J.H. Grove, C.S. Fowler, M.E. Sumner, Determination of the charge character of
890 selected acid soils, Soil Science Society of America Journal, 46 (1982) 32-38.

891 [50] D.L. Sparks, J.M. Bartels, J.M. Bigham, Part 3: Chemical Methods, Soil Science
892 Scociety of America, Madison, Wisconsin, 1996.

893 [51] AFNOR, NF X31-130: Détermination de la capacité d'échange cationique (CEC) et
894 des cations extractibles, in, Paris, 1999.

895 [52] C.A.J. Appelo, D. Postma, Geochemistry, Groundwater and Pollution, 2nd ed.,
896 Balkema, Leiden, Netherlands, 2005.

897 [53] I.B. Oliveira, A.H. Demond, A. Salehzadeh, Packing of sands for the production of
898 homogeneous porous media, Soil Science Society of America Journal, 60 (1996) 49-
899 53.

900 [54] Y. Mualem, New model for predicting hydraulic conductivity of unsaturated porous
901 media, WRR, 12 (1976) 513-522.

902 [55] M.T. van Genuchten, Closed-form equation for predicting the hydraulic conductivity
903 of unsaturated soils, Soil Science Society of America Journal, 44 (1980) 892-898.

904 [56] J. Šimůnek, M. Šejna, H. Saito, M. Sakai, M.T. van Genuchten, 2009. The HYDRUS-
905 1D software package for simulating the movement of water, heat, and multiple solutes
906 in variably saturated media, Version 4.0. Department of Environmental Sciences,
907 University of California Riverside: Riverside, California.

908 [57] M. Abramowitz, A.I. Stegun, Handbook of Mathematical Functions with Formulas,
909 Graphs, and Mathematical Tables, United States Department of Commerce, National
910 Bureau of Standards, Washington DC, 1972.

911 [58] O.A. Cirpka, P.K. Kitanidis, Numerical evaluation of solute dispersion and dilution in
912 unsaturated heterogeneous media, WRR, 38 (2002).

913 [59] T. Sato, H. Tanahashi, H.A. Loaiciga, Solute dispersion in a variably saturated sand,
914   WRR, 39 (2003).

915 [60] D. Schulze-Makuch, Longitudinal dispersivity data and implications for scaling
916   behavior, Ground Water, 43 (2005) 443-456.

917 [61] COMSOL Multiphysics®, 2011. Available from: http://www.comsol.com/, accessed
918   15.04.2011.

919 [62] S.R. Charlton, D.L. Parkhurst, Modules based on the geochemical model PHREEQC
920   for use in scripting and programming languages, Computers & Geosciences, In Press,
921   Accepted Manuscript (2010).

922 [63] MATLAB®, 2011. The MathWorks®, Available from: http://www.mathworks.com/,
923   accessed 15.04.2011.

924 [64] H. Prommer, D.A. Barry, G.B. Davis, A one-dimensional reactive multi-component
925   transport model for biodegradation of petroleum hydrocarbons in groundwater,
926   Environmental Modelling & Software, 14 (1999) 213-223.

927 [65] H. Prommer, D.A. Barry, C. Zheng, MODFLOW/MT3DMS-based reactive
928   multicomponent transport modeling, Ground Water, 41 (2003) 247-257.

929 [66] X. Mao, H. Prommer, D.A. Barry, C.D. Langevin, B. Panteleit, L. Li, Three-
930   dimensional model for multi-component reactive transport with variable density
931   groundwater flow, Environmental Modelling & Software, 21 (2006) 615-628.

932 [67] L. Wissmeier, D.A. Barry, Simulation tool for variably saturated flow with
933   comprehensive geochemical reactions in two- and three-dimensional domains,
934   Environmental Modelling & Software, 26 (2011) 210-218.

935 [68] E.P. Hodgkin, B.H. Hamilton, Fertilizers and eutrophication in Southwestern
936   Australia - Setting the scene, Fertilizer Research, 36 (1993) 95-103.

937 [69] J. Eastham, 2005. A simple water balance approach for estimating the amount of
938   leachate from bauxite residue storage areas. ALCOA World Alumina, Internal Report.

939 [70] I.R. Phillips, 2009. Guidelines for constructing a field lysimeter to monitor water-
940   nutrient-plant dynamics. ACOA World Alumina, Mining Environmental Group,
941   Internal Report.

942 [71] G.H. Buchanan, G.B. Winner, The solubility of mono and diammonium phosphate,
943   Journal of Industrial and Engineering Chemistry, 12 (1920) 448-451.

944 [72] K. Bajracharya, D.A. Barry, Analysis of one-dimensional multispecies transport
945   experiments in laboratory soil columns, Environment International, 21 (1995) 687-
946   691.

947 [73] D.A. Barry, J.L. Starr, J.Y. Parlange, R.D. Braddock, Numerical analysis of the snow-
948   plow effect, Soil Science Society of America Journal, 47 (1983) 862-868.

949 [74] C.A.J. Appelo, Multicomponent ion exchange and chromatography in natural
950   systems, in: P.C. Lichtner, C.I. Steefel, E.H. Oelkers (Eds.) Reactive Transport in
951   Porous Media, Mineralogical Society of America, Washington, 1996, pp. 193-227.

952 [75] J.W.C. Wong, G.E. Ho, Effects of gypsum and sewage sludge amendment on physical
953   properties of fine bauxite refining residue, Soil Science, 152 (1991) 326-332.

954 [76] J.W.C. Wong, G.E. Ho, Use of waste gypsum in the revegetation on red mud
955   deposits: A greenhouse study, Waste Management and Research, 11 (1993) 249-256.

956 [77] R. Mattinson, 2003. Assessment of amendments for sand residue neutralization,
957   Residue Neutralization. ALCOA World Alumina: Research and Development,
958   Internal Report.

959 [78] D.A. Rose, F. Konukcu, J.W. Gowing, Effect of watertable depth on evaporation and
960   salt accumulation from saline groundwater, Australian Journal of Soil Research, 43
961   (2005) 565-573.

962 [79] E. Shimojima, R. Yoshioka, I. Tamagawa, Salinization owing to evaporation from
963   bare-soil surfaces and its influences on the evaporation, J Hydrol, 178 (1996) 109-
964   136.

965 [80] C.E. Desborough, A.J. Pitman, P. Iranneiad, Analysis of the relationship between bare
966   soil evaporation and soil moisture simulated by 13 land surface schemes for a simple
967   non-vegetated site, Global and Planetary Change, 13 (1996) 47-56.

968 [81] C.M. Carter, H.A. van der Sloot, D. Cooling, A. van Zomeren, T. Matheson,
969   Characterization of untreated and neutralized bauxite residue for improved waste
970   management, Environmental Engineering Science, 25 (2008) 475-488.

971 [82] B.I. Whittington, Quantification and characterisation of hydrogarnet and cancrinite
972   present in desilication product by powder X-ray diffraction, 4th International Alumina
973   Quality Workshop, (1996) 413-422.

974 [83] B.I. Whittington, The chemistry of CaO and $Ca(OH)_2$ relating to the Bayer process,
975   Hydrometallurgy, 43 (1996) 13-35.

976 [84] K.W. Perrott, Surface charge characteristics of amorphous aluminosilicates, Clays and
977   Clay Minerals, 25 (1977) 417-421.

978 [85] D.A. Dzombak, F.M.M. Morel, Surface Complexation Modeling : Hydrous Ferric
979   Oxide, Wiley, New York, 1990.

980 [86] Y. Watanabe, H. Yamada, J. Tanaka, Y. Komatsu, Y. Moriyoshi, Ammonium ion
981   exchange of synthetic zeolites: The effect of their open-window sizes, pore structures,
982   and cation exchange capacities, Separation Science and Technology, 39 (2004) 2091-
983   2104.

984 [87] R.M. Barrer, Klinowsk.J, H.S. Sherry, Zeolite exchangers - Thermodynamic
985   treatment when not all ions are exchangeable, Journal of the Chemical Society-
986   Faraday Transactions, 69 (1973) 1669-1676.

987 [88] R.M. Barrer, R.P. Townsend, Ion-exchange equilibria in zeolites and clay-minerals -
988   Different concentration scales and derived thermodynamic functions, Journal of the
989   Chemical Society-Faraday Transactions, 80 (1984) 629-640.

990 [89] C. Colella, Ion exchange equilibria in zeolite minerals, Mineralium Deposita, 31
991   (1996) 554-562.

992   [90]   R.T. Pabalan, F.P. Bertetti, Cation-exchange properties of natural zeolites, in: Natural
993   Zeolites: Occurrence, Properties, Applications, 2001, pp. 453-518.

994   [91]   J.W.C. Wong, G.E. Ho, Cation exchange behavior of bauxite refining residues from
995   Western Australia, Journal of Environmental Quality, 24 (1995) 461-466.

996   [92]   J. Anderson, R.W. Bell, I.R. Phillips, Mobility of cations in bauxite residue sand
997   treated with residue fines, in: Joint Australian Society of Soil Science-New Zealand
998   Society of Soil Science Conference, Massey, New Zealand, 2008.

999   [93]   N.W. Menzies, I.M. Fulton, W.J. Morrell, Seawater neutralization of alkaline bauxite
1000   residue and implications for revegetation, Journal of Environmental Quality, 33
1001   (2004) 1877-1884.

1002   [94]   C. Hanahan, D. McConchie, J. Pohl, R. Creelman, M. Clark, C. Stocksiek, Chemistry
1003   of seawater neutralization of bauxite refinery residues (red mud), Environmental
1004   Engineering Science, 21 (2004) 125-138.

1005   [95]   J. Eastham, T. Morald, P. Aylmore, Effective nutrient sources for plant growth on
1006   bauxite residue: I. Comparing organic and inorganic fertilizers, Water, Air, and Soil
1007   Pollution, 176 (2006) 5-19.

1008   [96]   R.D. Fuller, E.D.P. Nelson, C.J. Richardson, Reclamation of Red Mud (Bauxite
1009   Residues) using alkaline-tolerant grasses with organic amendments, Journal of
1010   Environmental Quality, 11 (1982) 533-539.

1011   [97]   J.W.C. Wong, G. Ho, Sewage-sludge as organic ameliorant for revegetation of fine
1012   bauxite refining residue, Resources, Conservation and Recycling, 11 (1994) 297-309.

1013   [98]   J. Eastham, T. Morald, Effective nutrient sources for plant growth on bauxite residue:
1014   II. Evaluating the response to inorganic fertilizers, Water, Air, and Soil Pollution, 171
1015   (2006) 315-331.

1016   [99]   J.C. van Dam, R.A. Feddes, Numerical simulation of infiltration, evaporation and
1017   shallow groundwater levels with the Richards equation, J Hydrol, 233 (2000) 72-85.

1018   [100]   E.G. Lappala, R.W. Healy, E.P. Weeks, 1987. Documentation of computer program
1019   VS2D to solve the equations of fluid flow in variably saturated porous media. U.S.
1020   Geological Surfay: Denver, Colorado.

1021   [101]   COMSOL Multiphysics®, 2008. Pesticide transport and reaction in soil, Earth Science
1022   Module Model Library.

1023   [102]   I. Kosztin, B. Barz, L. Janosi, Calculating potentials of mean force and diffusion
1024   coefficients from nonequilibrium processes without Jarzynski's equality, Journal of
1025   Chemical Physics, 124 (2006) -.

1026   [103]   J. Li, M. Hesse, J. Ziegler, A.W. Woods, An arbitrary Lagrangian Eulerian method for
1027   moving-boundary problems and its application to jumping over water, Journal of
1028   Computational Physics, 208 (2005) 289-314.

1029   [104]   H.J. Vogel, O. Ippisch, Estimation of a critical spatial discretization limit for solving
1030   Richards' equation at large scales, Vadose Zone Journal, 7 (2008) 112-114.

1031　[105]　Wolfram MathWorld, 2011. Heaviside step function, Available from:
1032　　　　http://mathworld.wolfram.com/HeavisideStepFunction.html, accessed 15.04.2011.

1033

1034

Appendix A: Sequential Solution of Flow and Transport

1036　Using the coupling of COMSOL and IPhreeqc, the simultaneous solution of the non-linear

1037　partial differential equation of variably saturated flow together with numerous transport

1038　equations for multi-component solutions in complex domains quickly becomes unstable with

1039　excessive memory requirements. In order to increase the efficiency and stability of COMSOL

1040　computations, flow and transport were solved sequentially using COMSOL's segregated

1041　solver. This assumes a strict one-way coupling between the two processes. Thus, the iterative

1042　solution of Richards' equation is only computed for the pressure variable. The resulting time-

1043　dependent flow field is then input into the multi-component solute transport equations, which

1044　are linear and thus easier and faster to solve.

Appendix B: Parallelization

1046　During reaction calculations in IPhreeqc, each node of the discretized simulation domain is

1047　represented by an independent geochemical batch system. Thus, large domains require the

1048　computation of several thousands of batch systems, which may lead to long computation

1049　times particularly if complex kinetic reactions are involved. For increased computational

1050　efficiency, reaction calculations were parallelized, making use of MATLAB's *single program*

1051　*multiple data* algorithm. In this procedure, an IPhreeqc COM-object is initialized on each of

1052　the engaged processors and the number of batch systems for evaluation is distributed evenly.

1053   The speed increase that results from distributed reaction calculations scales well with the

1054   number of available processors.

1055 Appendix C: Implementation of Atmospheric and Seepage Face Boundaries

1056   The interface for Richards' equation in COMSOL's Earth Science Module provides

1057   predefined settings for pressure head and flux boundary conditions. In the case of seepage

1058   face and atmospheric boundaries, however, a flux condition may turn locally into a head

1059   condition and vice versa according to a head-based criterion [e.g., 99, 100]. Since the type of

1060   boundary condition cannot be changed during a simulation, the stiff-spring approach, where a

1061   Neumann statement about flux is used to achieve a Dirichlet condition for the pressure head,

1062   has to be employed [101].

1063   A seepage face boundary conceptualizes a porous medium that drains freely and where the

1064   out-flowing water is removed rapidly enough such that it does not build up on the surface.

1065   Consequently, a zero head condition applies as long as there is potential outflow from the

1066   domain (the pressure head within the domain is greater than zero). In unsaturated conditions

1067   (negative pressure head), the boundary turns into a no-flow boundary. The stiff-spring

1068   representation of a seepage face boundary is given by

$$q_0 = \begin{cases} 0, & H_0 \leq 0 \\ -k_{sp}H_0, & H_0 > 0 \end{cases} \qquad \text{(C.1)}$$

1069   where q_0 (m s^{-1}) is the inward flux crossing the boundary, H_0 (m) is the actual pressure head

1070   at the boundary and k_{sp} (s^{-1}) is the positive spring constant. The flux $-k_{sp}H_0$ must be of a

1071   magnitude sufficient to prevent build-up of water and fix the pressure head at the boundary

1072   effectively to zero. Therefore, the accuracy of the stiff-spring representation increases with

1073   the magnitude of k_{sp}, however at the cost of numerical efficiency and stability [102, 103].

1074 Atmospheric boundary conditions are governed by the recharge flux $r(t)$ (m s^{-1}), which is the

1075 difference between the absolute values of rainfall and potential evaporation. In the case of

1076 bare soil evaporation, $r(t)$ is limited by the water availability in the soil. Once a critical

1077 negative pressure head, H_{crit} (m), at the soil surface is reached, the boundary conceptually

1078 switches from a specified flux boundary to a head condition. H_{crit} is the pressure potential of

1079 the atmosphere and a measure of the atmospheric evaporation demand [100]. In dry and hot

1080 weather situations, it may exceed in magnitude -10^3 m. Thus, in contrast to the seepage face

1081 boundary, the change between constant head and specified flux occurs in the dry range of the

1082 moisture spectrum, where H_0 is extremely sensitive to the applied flux. In order to avoid

1083 oscillations of the numerical scheme a smooth spring function is required that merges

1084 seamlessly with the flux in unconstrained conditions. For the representation of evaporation

1085 boundaries, we therefore make use of the following condition:

$$q_0 = -r(t) \tanh\left[\frac{\xi}{r(t)}(H_0 - H_{crit})\right], \tag{C.2}$$

1086 where ξ (T^{-1}) is the derivative of q_0 with respect to H at H_{crit}, which determines implicitly

1087 the width of the transition zone between unconstrained and limited evaporation.

1088 **Fig. 17: Boundary flux during negative recharge in the vicinity of the critical pressure head H_a.**

1089 The behaviour of q_0 in the vicinity of H_{crit} is illustrated in Fig. 17. As H_0 approaches H_{crit},

1090 the magnitude of the evaporation flux is reduced continuously until evaporation stops

1091 completely and even gives positive values (condensation) if H_{crit} is surpassed. This

1092 behaviour is consistent with the physical process, where evaporation from dry soils is

1093 gradually reduced due to limited water availability. Low values of H_{crit} require a larger

1094 smoothing zone (lower ξ) and very fine domain discretization near the boundary [104] in

1095 order to achieve numerical convergence.

1096   In the case of positive recharge the boundary flux is limited by the infiltration capacity at the

1097   maximum surface pressure head H_{po} (m), which represents the maximum height of ponded

1098   water [56]. Conceptually, the specified flux condition $q_0 = r(t)$ turns into a head condition

1099   when H_0 exceeds H_{po}. This can be expressed as a conventional stiff-spring boundary

1100   according to:

$$q_0 = \begin{cases} r(t), & H_0 \leq H_{po} \\ r(t) - k_{po}(H_0 - H_{po}), & H_0 > H_{po} \end{cases}, \tag{C.3}$$

1101   where k_{po} (s^{-1}) is the spring constant. The flux $-k_{po}(H_0 - H_{po})$ reduces infiltration until the

1102   ponded boundary head is established.

1103   The full atmospheric boundary condition results from combining the evaporation boundary

1104   Eq. (C.2) with the infiltration boundary Eq. (C.3), yielding:

$$q_0 = \begin{cases} -r(t)\tanh\left[\dfrac{\xi}{r(t)}(H_0 - H_{crit})\right], & r(t) < 0 \\ r(t)\mathcal{H}(H_{po} - H_0) + \left[r(t) - k_{po}(H_0 - H_{po})\right]\mathcal{H}(H_0 - H_{po}), & r(t) \geq 0 \end{cases}, \tag{C.4}$$

1105   where $\mathcal{H}$ is the Heaviside step function [e.g., 105].

1106   Instead of the tanh-function in Eq. (C.4), COMSOL's smoothed version of the Heaviside

1107   function *flc2hs* can be used. The inwards recharge flux then becomes

$$q_0 = r(t)[-1 + 2\,flc2hs(H_0 - H_{crit}, \varrho)], \qquad r(t) < 0. \tag{C.5}$$

1108   In Eq. (C.5) the transition zone is explicitly determined by the parameter ϱ (m). However the

1109   slope of q_0 with respect to H_0 at H_{crit}, which is relevant for numerical stability, depends on

1110 H_{crit} and q_0.

Appendix D: Particle Size Distribution, Surface Area

1111

1112 It is generally accepted that the rate of mineral reactions is proportional to the area of the

1113 reacting surface [45, 52]. In order to determine the macroscopic surface area a particle-size

1114 analysis was performed on washed residue sand (see Section 2.2 for details on washing

1115 procedure) using laser diffraction particle size analysis (LS 13 320 Beckman Coulter). In Fig.

1116 18, the relative solid volume against particle diameter is displayed as the mean of four

1117 replicates.

1118 **Fig. 18: Particle size distribution of washed residue sand.**

1119 With the assumption of spherical particles and a measured solid density of 2.74 g cm^{-3} the

1120 specific surface area of residue sand, as derived from the particle size distribution, amounts to

1121 0.0264 m^2 g^{-1}.
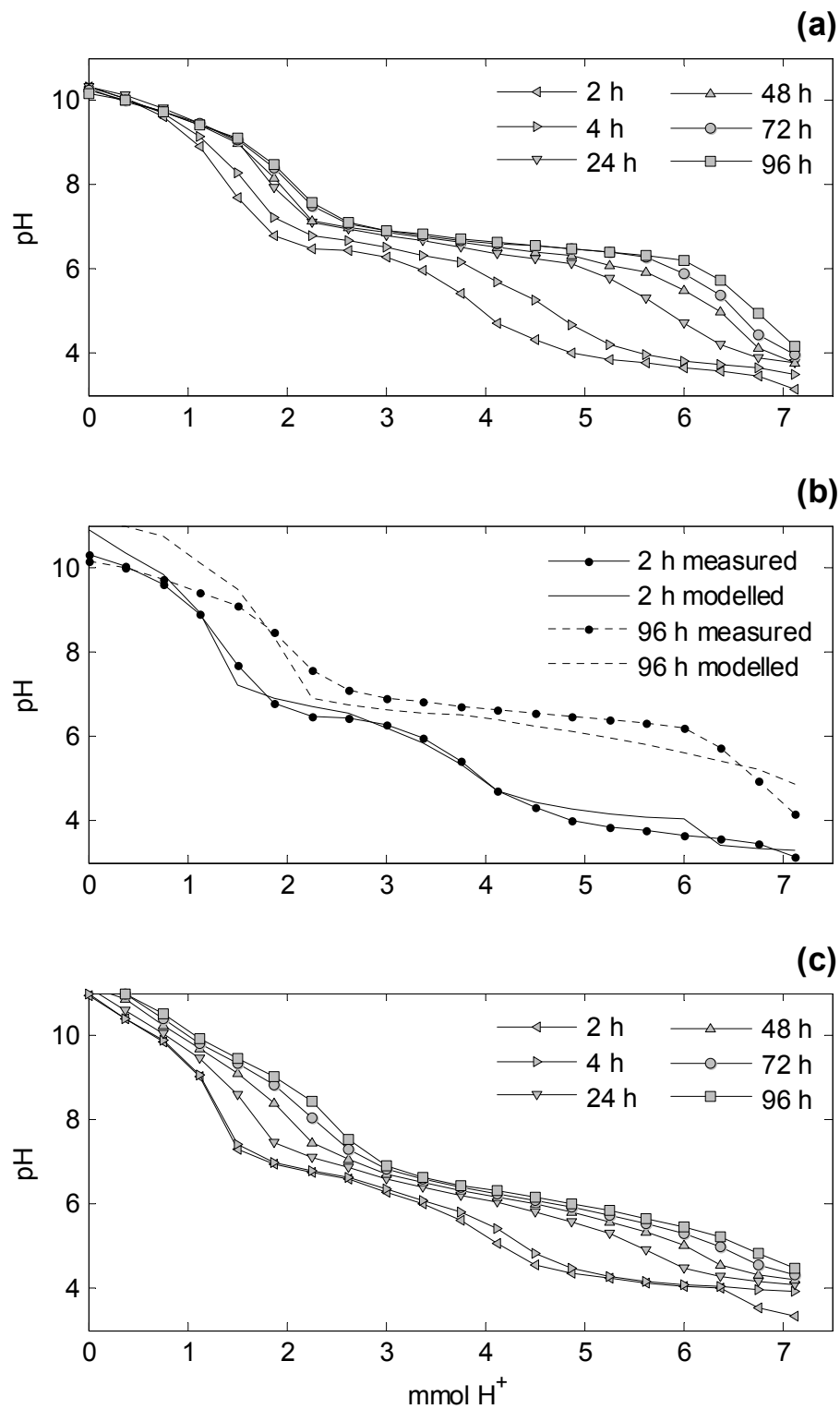
Fig. 1: Measured (a) and simulated acid neutralization curves at thermodynamic equilibrium (b) and including the kinetic dissolution of TCA and sodalite (c).
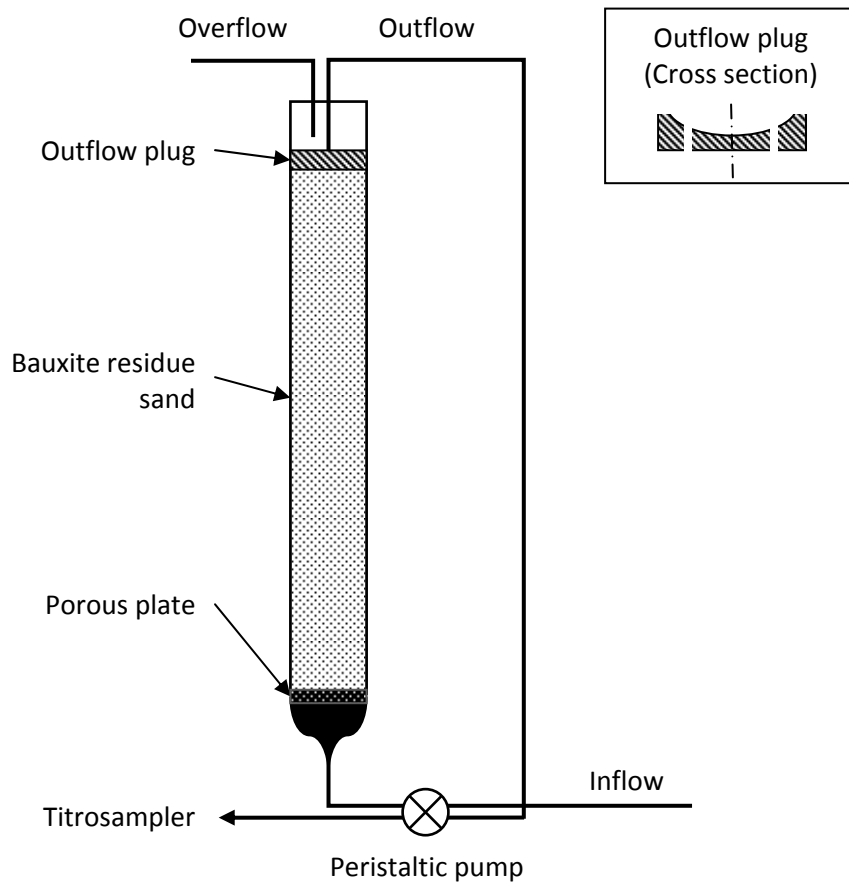
Fig. 2: Upward flow column experiment.
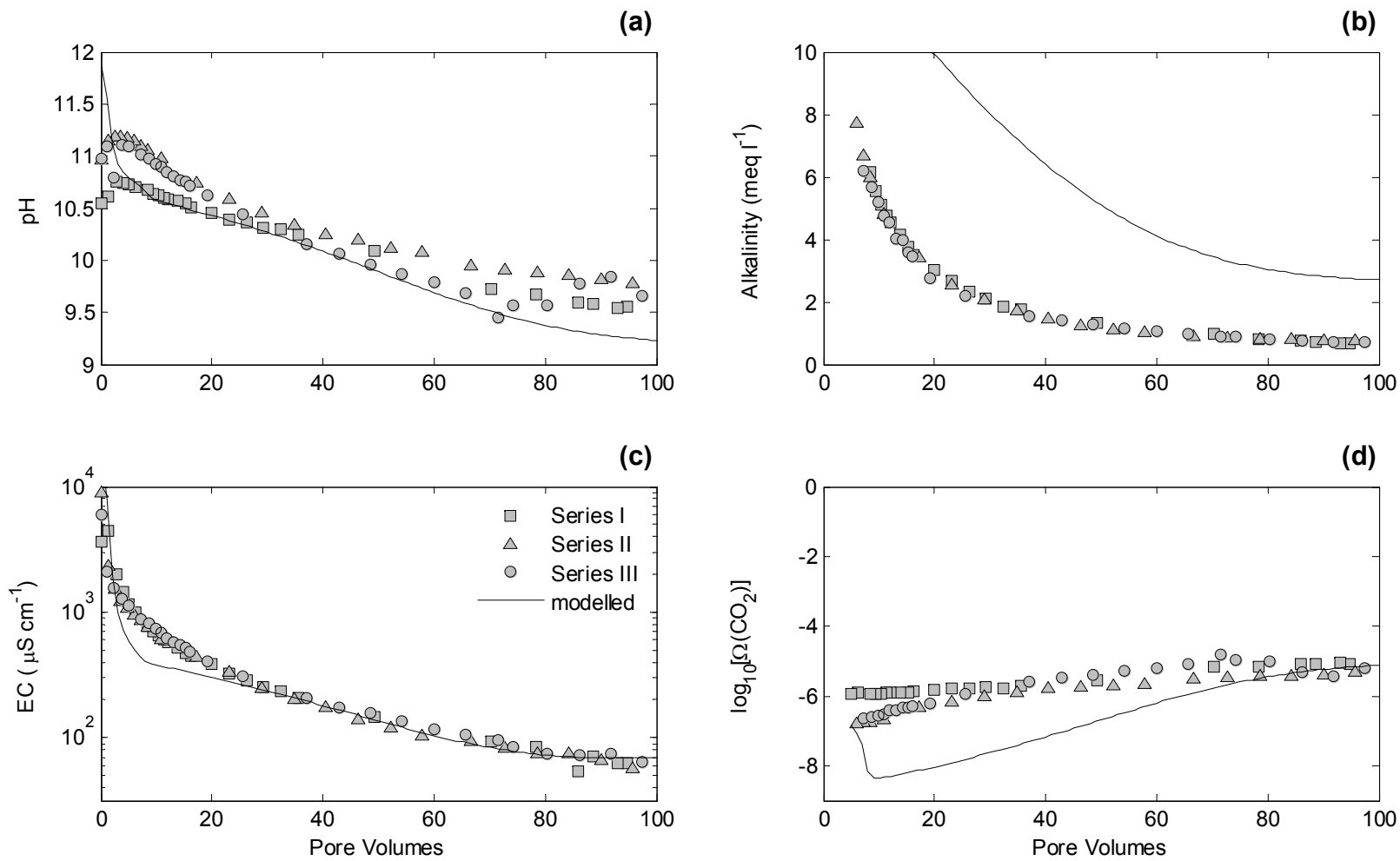
Fig. 3: Results of column experiment for pH (a), alkalinity (b), electrical conductivity (c) and calculated CO₂ saturation (d).
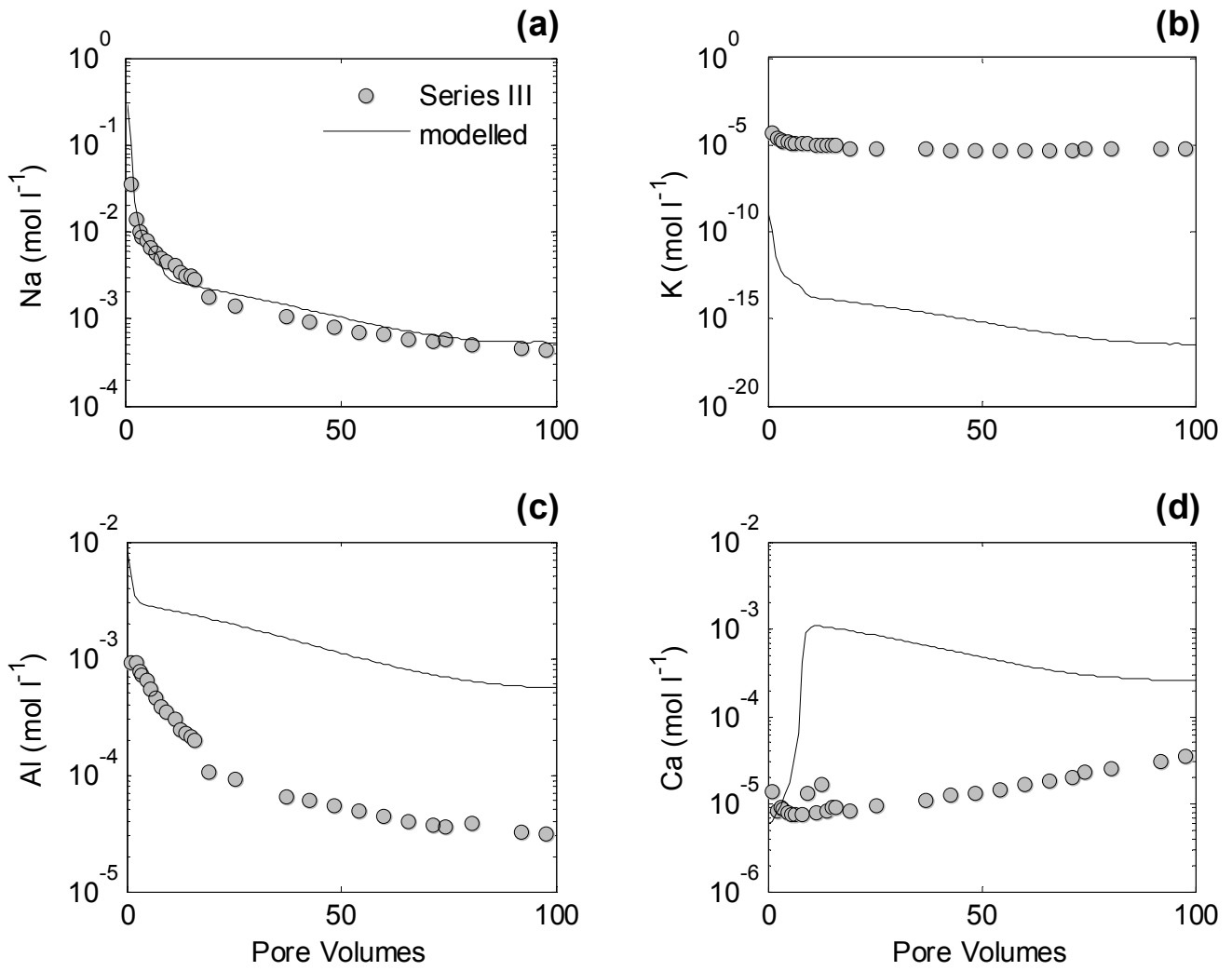
Fig. 4: Element concentrations (mol l^{-1}) in the column outflow for (a) Na, (b) K, (c) Al and (d) Ca.
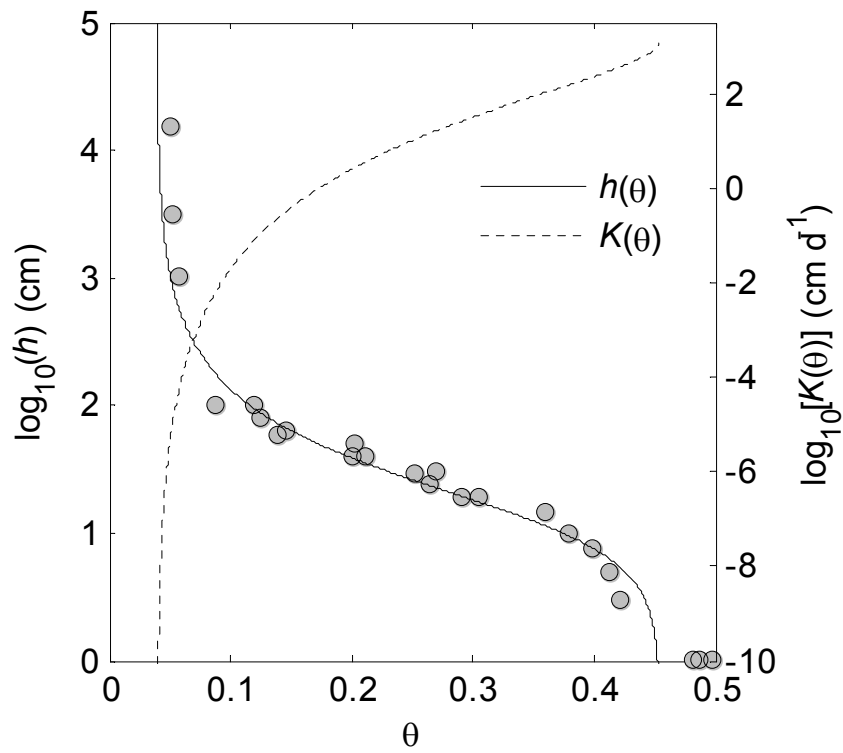
Fig. 5: Water retention and unsaturated hydraulic conductivity of residue sand at the soil surface according to the van Genuchten/Mualem model.

Fig. 6: Depth dependence of saturated hydraulic conductivity K_s (left) and saturated water content θ_s (right).

Matlab®

Domain Geometry
Domain Discretisation (Meshing)
Flow and Transport Properties
Boundary and Initial Conditions
PHRREQC Reaction Properties

COMSOL®

Aqueous Phase Flow

Flow Velocities
Moisture Content

Solute Transport

Master Species Concentrations
Moisture Content

IPhreeqc (COM version)

Reactions
Intra-phase Speciation
Inter-phase Speciation
Kinetic Reactions

Element Concentrations
Mass of Water

Split-Operator Time Step Δt

Post-processing
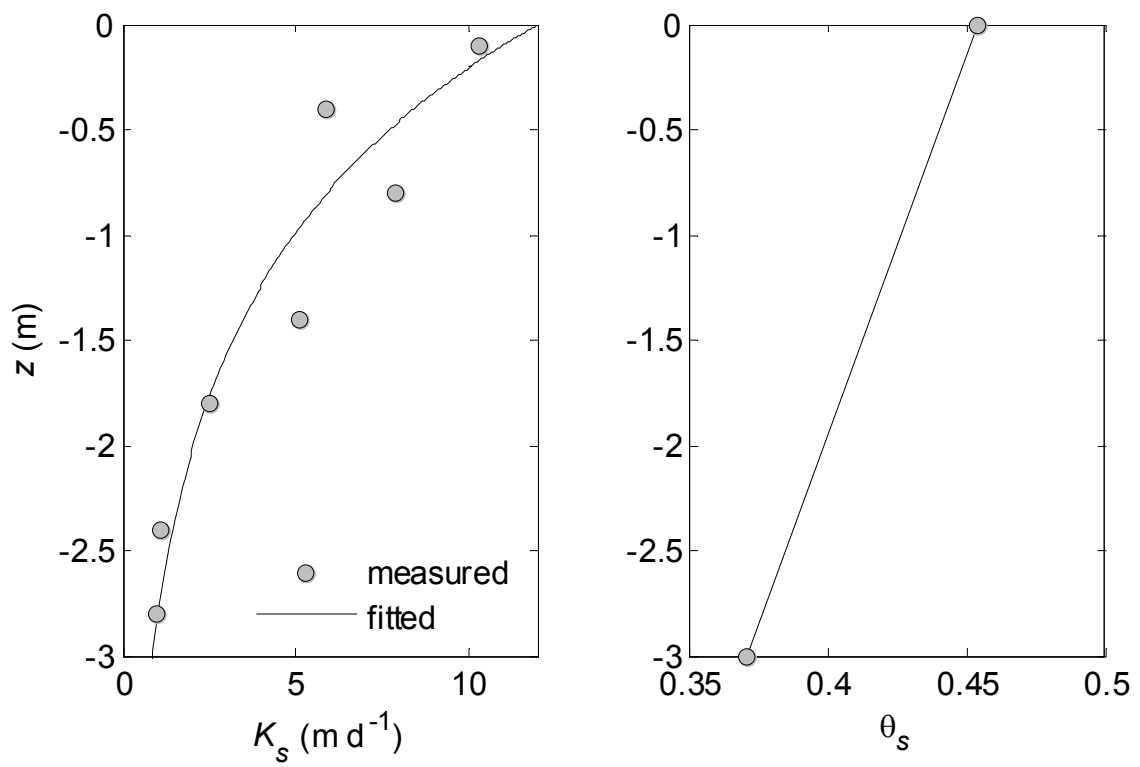
Fig. 7: Program flow and structure.
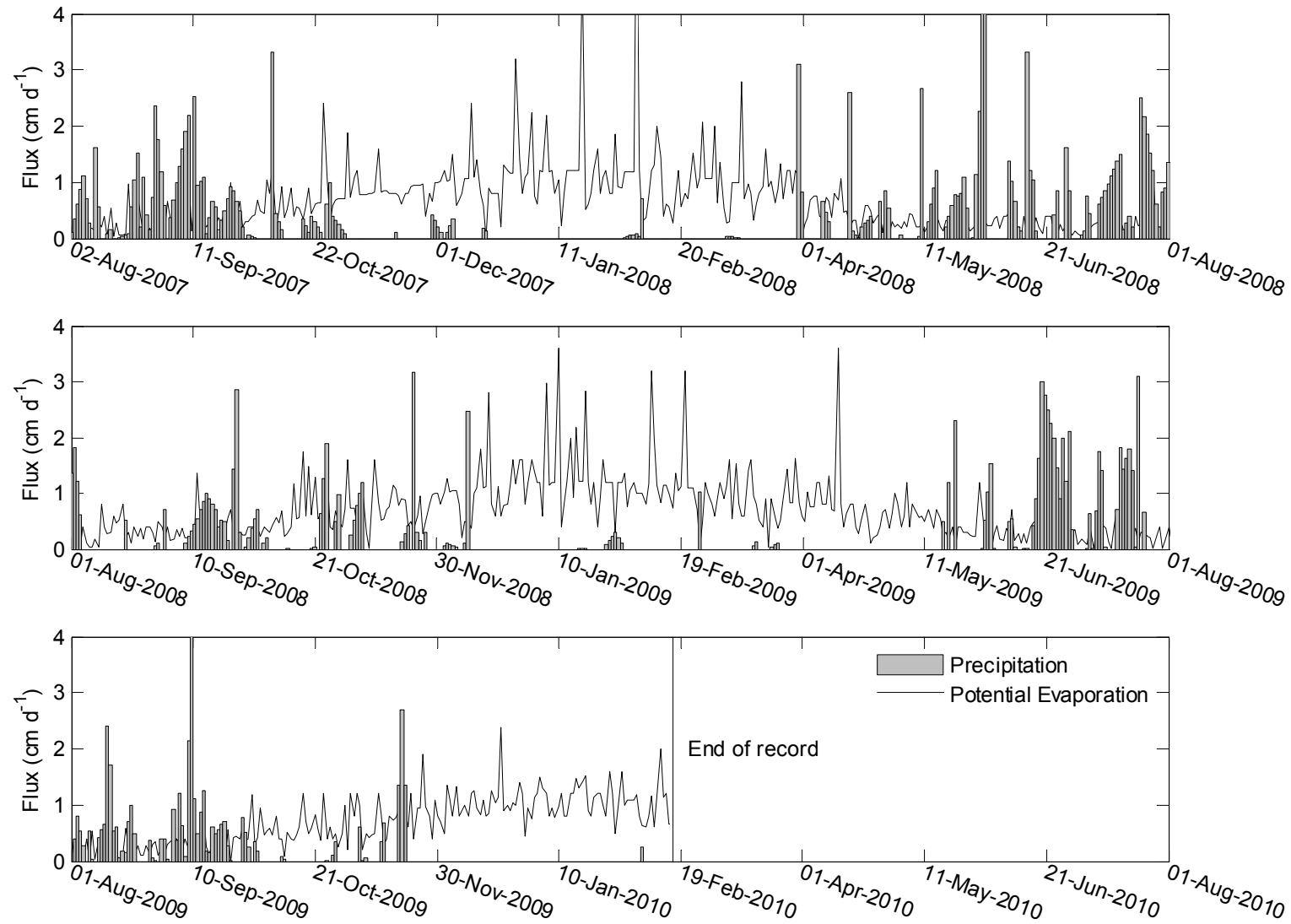
Fig. 8: Time series of rainfall and potential evaporation with reconstructed missing values.
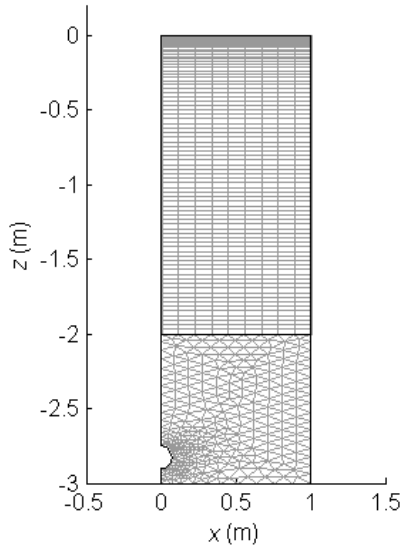
Fig. 9: Lysimeter simulation domain and finite element representation.
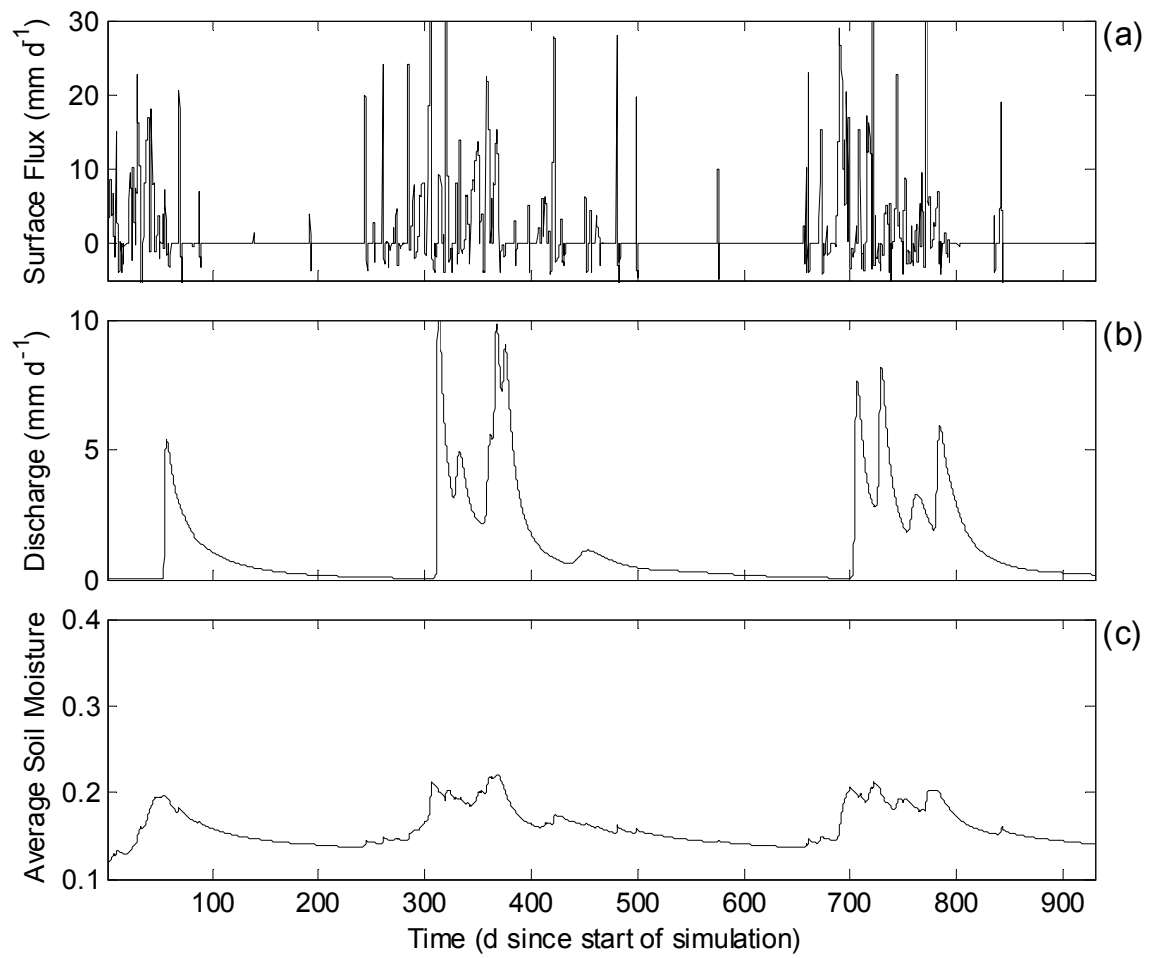
Fig. 10: Dynamic water balance of lysimeter simulation with (a) surface flux (mm d^{-1}), (b) drainage at the drainage pipe (mm d^{-1}) and (c) average soil moisture content θ.
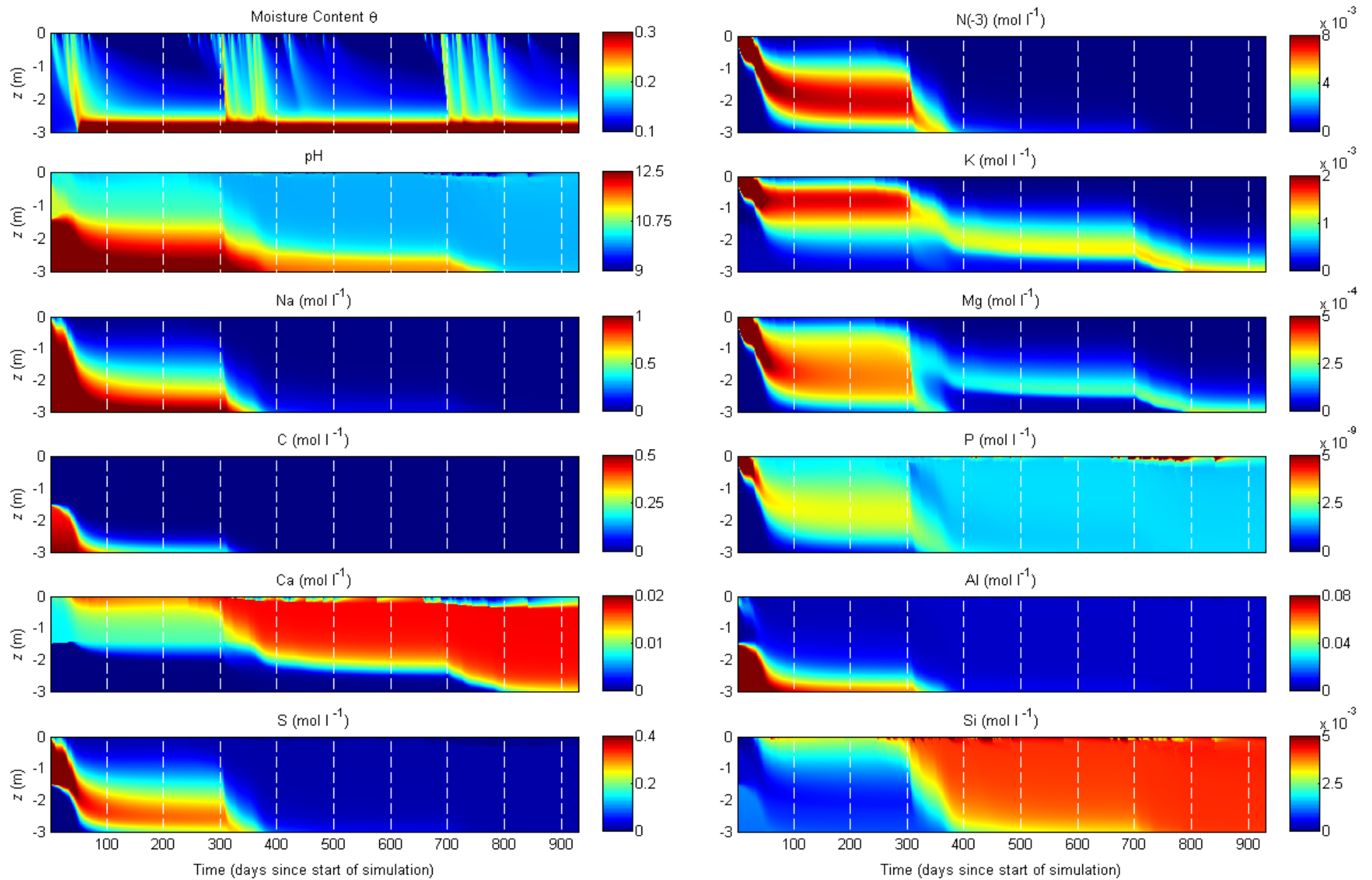
Fig. 11: Evolution of moisture content, pH and concentration of selected elements at the right domain boundary of the lysimeter simulation.
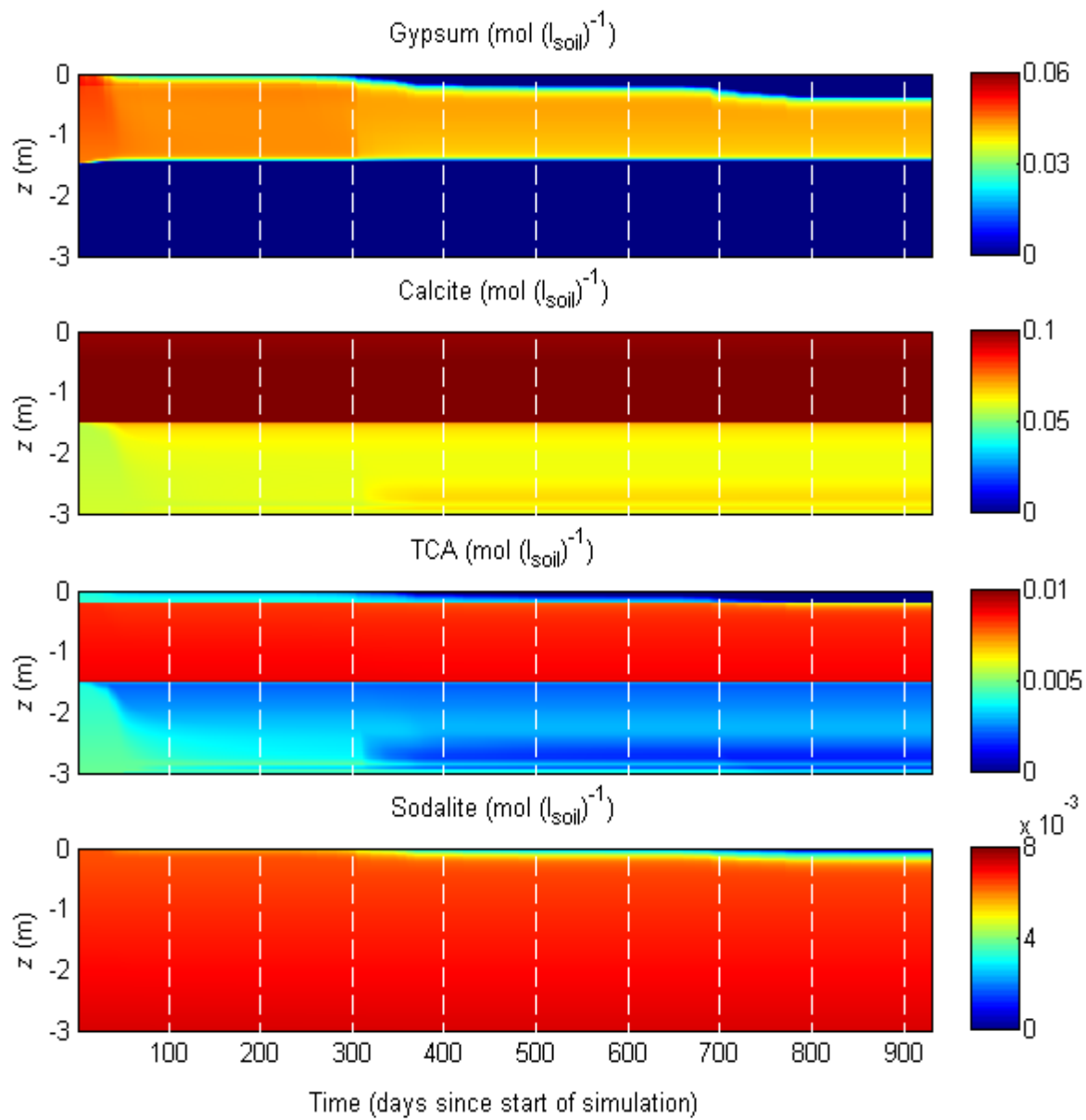
Fig. 12: Evolution of the main minerals at the right domain boundary of the lysimeter simulation.
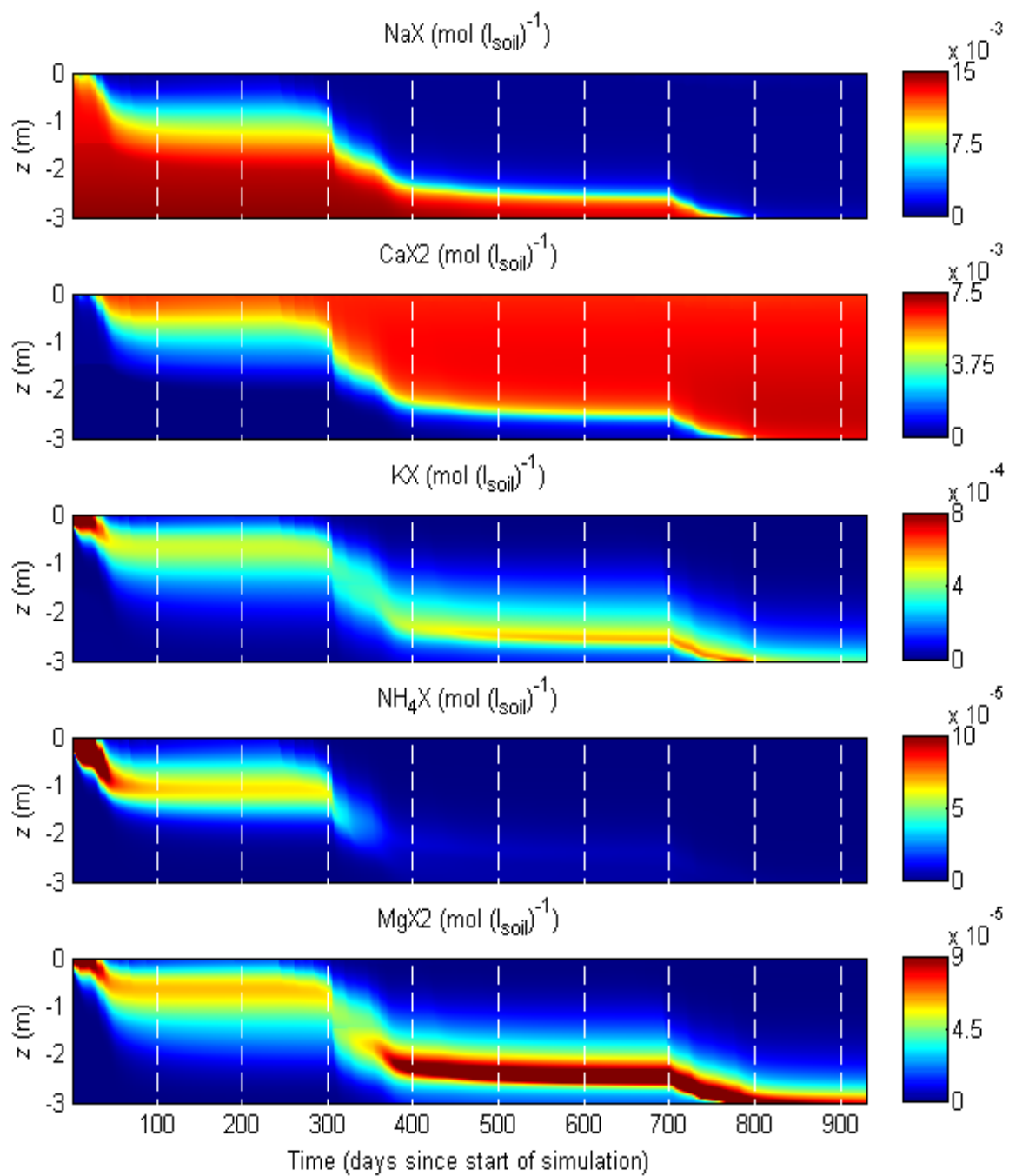
Fig. 13: Evolution of the exchanger composition at the right domain boundary of the lysimeter simulation.
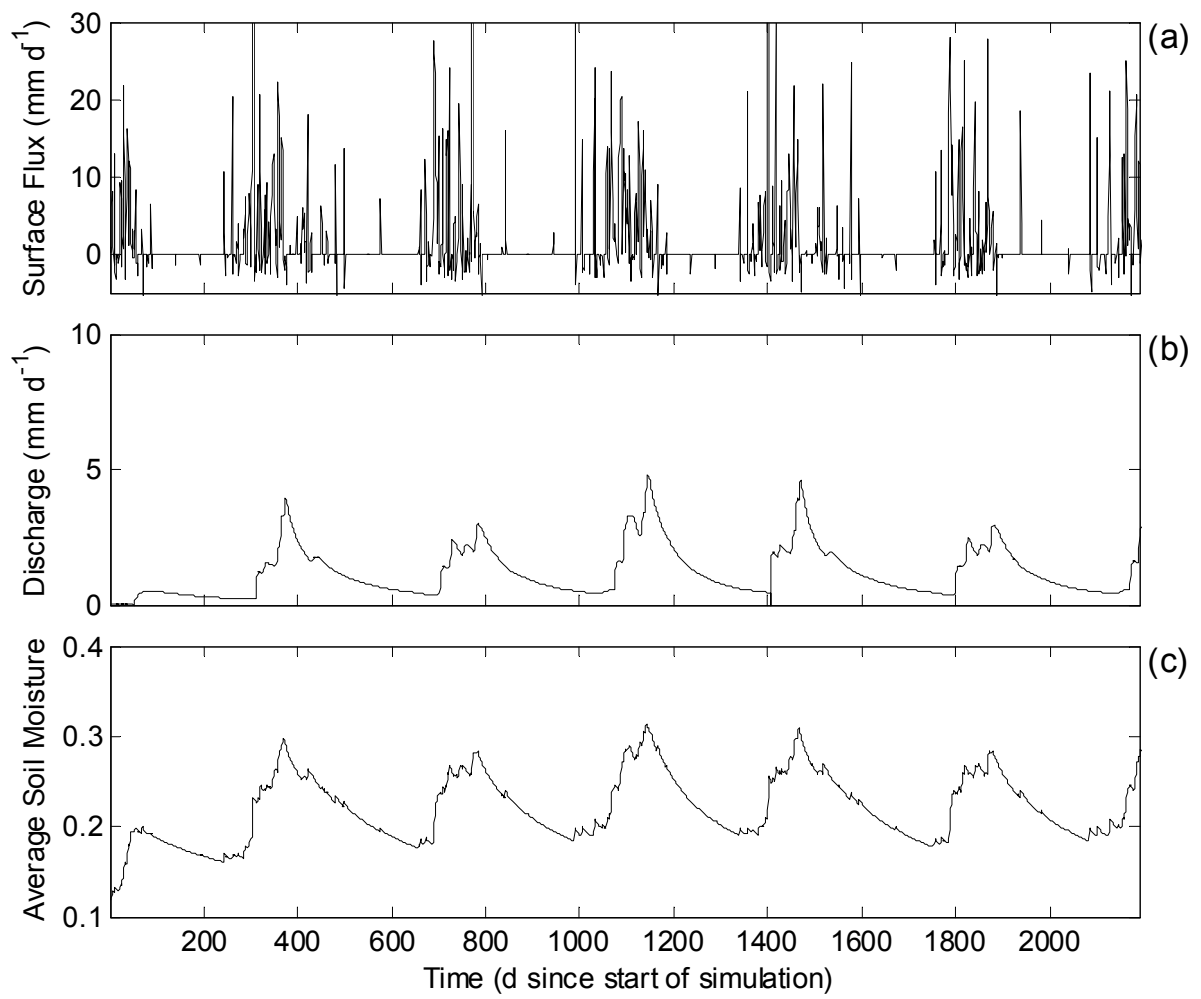
Fig. 14: Dynamic water balance of surface cover simulation, with (a) surface flux (mm d^{-1}), (b) drainage (mm d^{-1}) and (c) average soil moisture content θ.
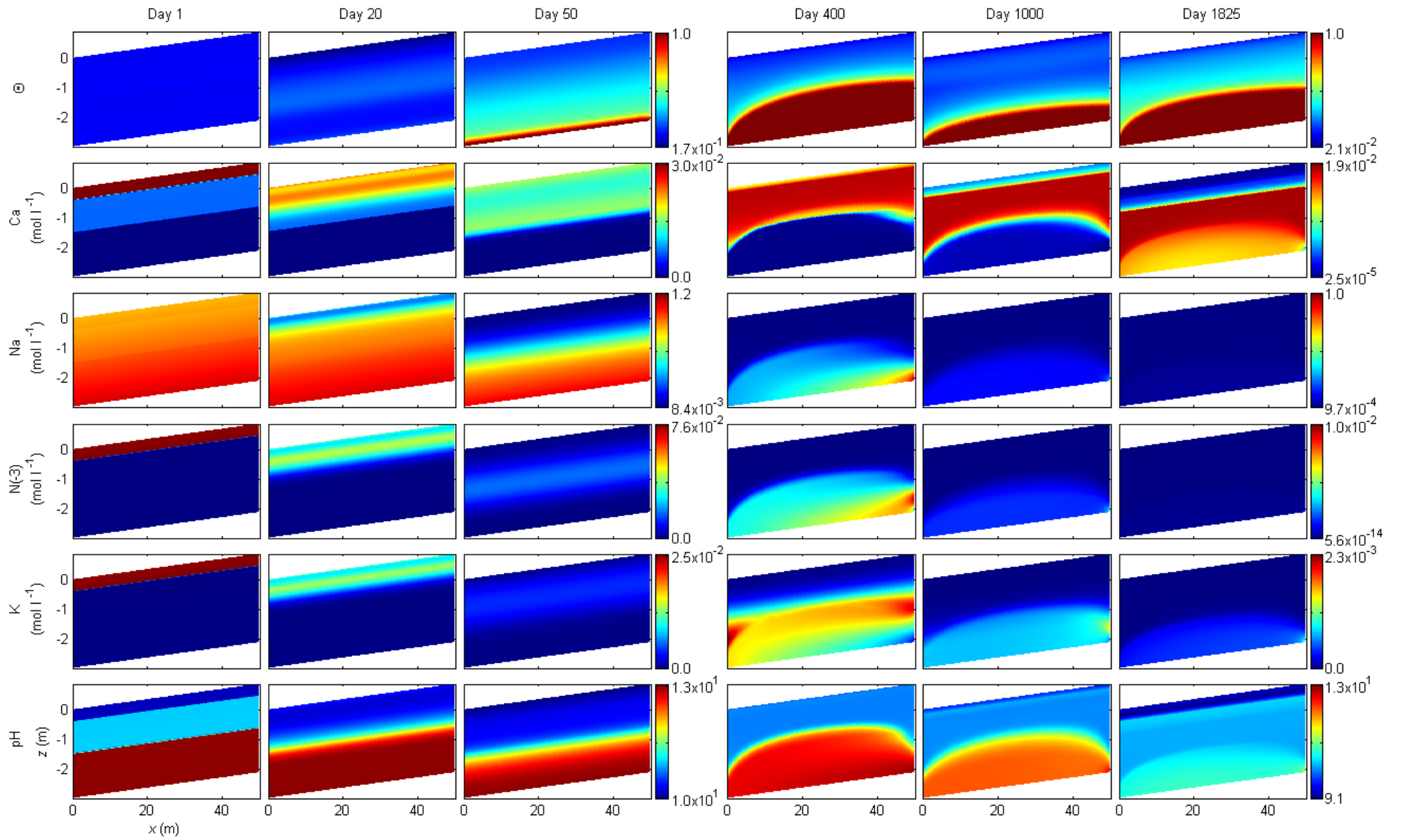
Fig. 15: Evolution of normalized moisture content, concentrations of selected elements and pH profiles of the surface cover simulation at 1, 20, 50, 400, 600 and 1825 d.
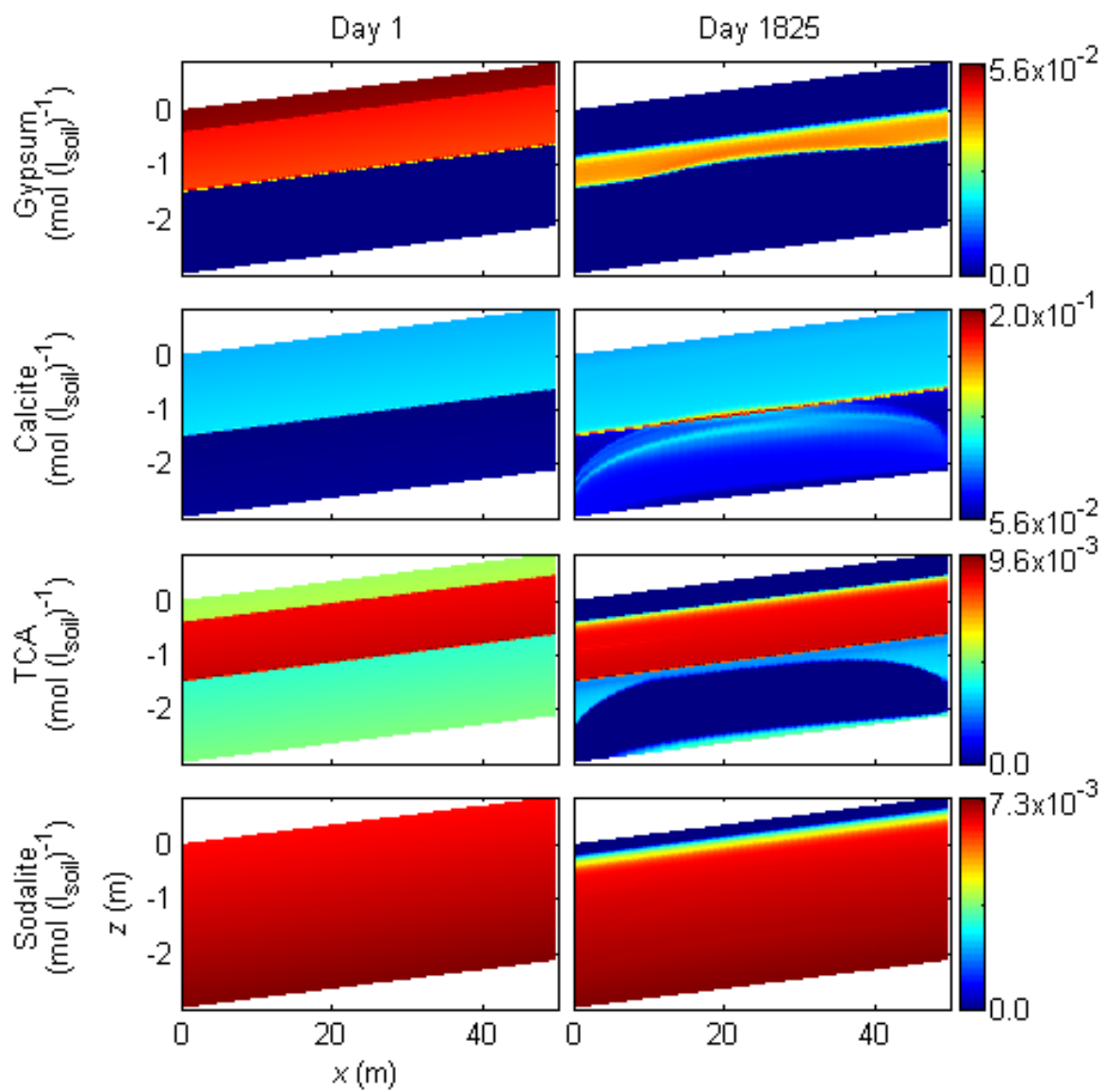
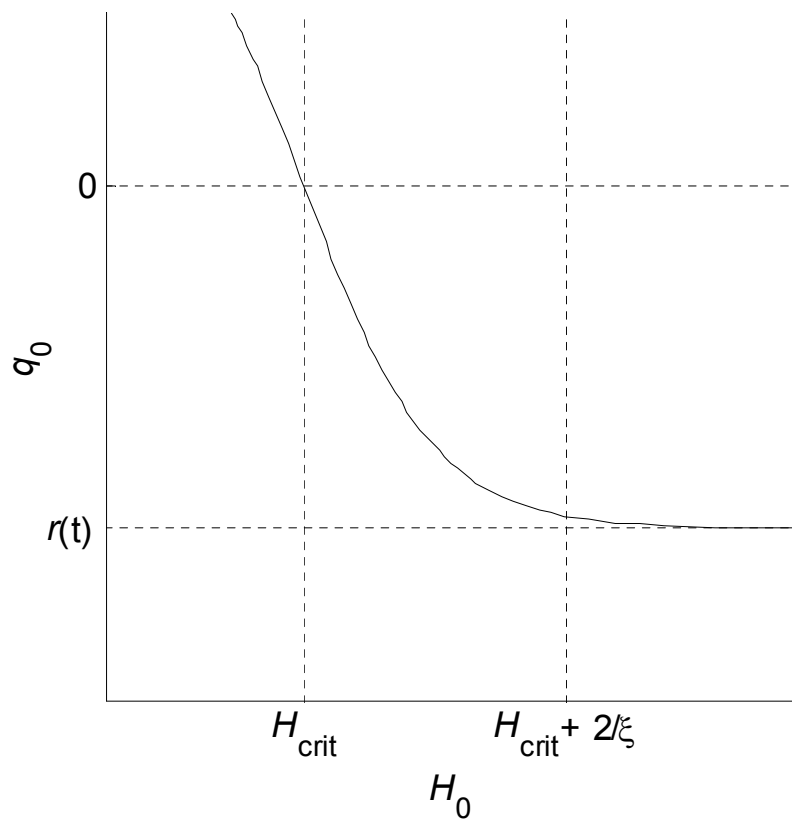Fig. 16: Evolution of the main minerals of the surface cover simulation for 1 and 1825 d.

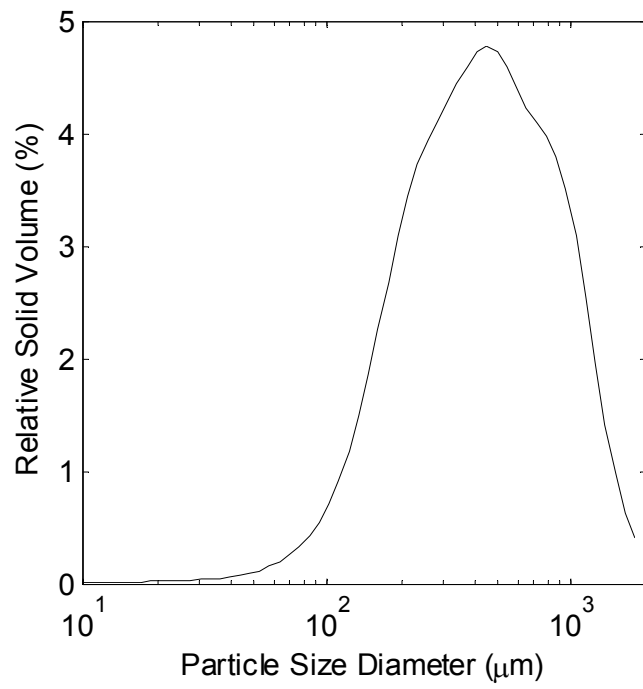Fig. 17: Boundary flux during negative recharge in the vicinity of the critical pressure head H_a.

Fig. 18: Particle size distribution of washed residue sand.